Environmental Fluid Mechanics (2022) 22:921–954
https://doi.org/10.1007/s10652-022-09870-5

ORIGINAL ARTICLE

Experimental investigation of the near-surface flow dynamics in downburst-like impinging jets

Federico Canepa[1,2] · Massimiliano Burlando[1] · Djordje Romanic[1,2,3] · Giovanni Solari[1] · Horia Hangan[2,4]

Received: 3 December 2021 / Accepted: 2 May 2022 / Published online: 30 May 2022

Abstract

Downbursts are strong downdrafts that originate from thunderstorm clouds and create vigorous radial outflows upon hitting the ground. This study is part of the comprehensive experimental research on downburst outflows produced as large-scale impinging jets in the WindEEE Dome simulator at Western University, Canada. The 2800 tests carried out form the largest database of experimental measurements on downburst winds developed thus far, which is made available to the public in its whole and described in detail in a complementary study. Therefore, the current manuscript merely focuses on the data post-processing outcomes and interpretation of results from a selected subset of measurements. Impinging jets are here simulated as transient phenomena in which velocity time series are characterized by a sudden ramp-up of velocity, followed by the velocity peak, a short statistically stationary region, and the final velocity slowdown, as it is expected to occur in the actual downbursts. A dominant velocity peak that was systematically observed in all velocity records is associated with the radial advection of the primary vortex in the outflow. Depending on the radial distance from the downdraft, the primary vortex was sometimes preceded by a secondary, much smaller, vortex close to the surface. Vertical profiles of mean velocity and turbulence intensity are for the first time characterized through the extent of a downburst-like event in the spatiotemporal domain. Particularly, these profiles rapidly change in relation to the passage of the primary vortex and consequent variation of the surface layer thickness. This study lays out a foundation for an experimental model of non-stationary downburst outflows to come.

✉ Federico Canepa
federico.canepa@edu.unige.it

[1] Department of Civil, Chemical and Environmental Engineering (DICCA), Polytechnic School, University of Genoa, Via Montallegro 1, 16145 Genoa, Italy

[2] Wind Engineering, Energy and Environment (WindEEE) Research Institute, Western University, 2535 Advanced Avenue, London, ON N6M 0E2, Canada

[3] Department of Atmospheric and Oceanic Sciences, Faculty of Science, McGill University, Burnside Hall, 805 Sherbrook Street West, Montreal, QC H3A 0B9, Canada

[4] Faculty of Engineering and Applied Science, Ontario Tech University, 2000 Simcoe Street North, Oshawa, ON L1G 0C5, Canada

Article highlights

- Large experimental campaign and public database of measurements on transient downburst-like impinging jets.
- Characterization of the spatiotemporal evolution of wind speed and turbulence profiles.
- Measuring the effects of the primary and secondary vortices in the outflow on velocity and turbulence profiles.

Keywords Downburst · Impinging jet · Turbulence · Transient wind · Vortex structure

1 Introduction

Due to their importance in various fields of engineering and atmospheric sciences, impinging jets (IJs) have vastly been investigated over the last several decades [1–7]. This study focuses on the investigation of experimentally produced IJs with application to downburst outflows in nature. Downbursts develop from thunderstorm clouds when the falling rain and hail, associated with the evaporation and melting of hydrometeors inside and underneath the cloud, produces a strong downward current of negatively buoyant air. Once the downdraft hits the surface, the wind speeds in the radially expanding outflow can exceed 75 m s^{-1} [8] in the first 50–100 m from the surface. These high wind speeds can pose a serious hazard to people, structures and the environment. The complex characterization of downburst winds arises from their very limited temporal and spatial scales, respectively in the order of 10 min [9, 10] and few kilometers in diameter [9]. This makes downbursts small-scale, highly three dimensional (3D) and unsteady flows, and causes the full-scale recording of the complete phenomenon to be hardly practicable. Fujita [11] classified downbursts into microbursts (< 4 km) and macrobursts (> 4 km) based on the spatial extent of the outflow. Physical wind simulators need to be sufficiently large to replicate downburst outflows at reasonable geometric, velocity, and time scales. For example, an IJ of $\mathcal{O}$(1 m) with a geometric scale of 1:1000 and a velocity scale of 1:1 results in a time scale of 1:1000. Therefore, an actual downburst that lasts for 10 min in the atmosphere needs to be shorter than 0.6 s in the laboratory setting to satisfy the prescribed time scale. Besides, the region of the maximum horizontal velocities in the actual outflow, $\mathcal{O}$(100 m), reduces to the lowest ~ 1 cm from the wind tunnel floor given the above geometric scale. This small distance from the floor makes the punctual velocity measurements in this region technically challenging and unreliable.

The first field measuring campaigns [9, 11–13] used anemometers and Doppler radars to characterize downburst outflows. Full-scale measurements have become more and more frequent over the last several decades [14–19] and have employed the latest generation of downburst measuring techniques. These new datasets, such as the one presented in [10], facilitate more thorough analysis of both mean and turbulent characteristics of downburst flows and provided additional climatological descriptions of these wind events. In parallel with the field measurements, downbursts have also been investigated computationally using IJ models [20, 21], cloud and sub-cloud models [22–24] as well as mesoscale weather forecasting models [25]. While numerical models offer large diversity of results, flexibility and repeatability of the experiments under the same or different conditions, they often lack the proper representation of turbulence, instabilities, and coarse spatial and time resolutions to accurately represent all aspects of downburst outflows.

Physical simulations of downbursts in wind simulators mainly follow two experimental approaches: (1) buoyancy-driven currents; or (2) momentum-driven IJs. The former are typically called gravity currents [26–30], while the latter are simply referred to as IJs [31–35]. Our

literature survey indicates that the number of experimental studies on downbursts is smaller than the number of either numerical or full-scale research on downburst winds. This discrepancy is partially due to the limitations of traditional atmospheric boundary layer (ABL) wind tunnels to replicate highly 3D and non-stationary wind systems, such as thunderstorm downburst winds. At the same time, the facilities that are capable of creating downburst-like IJs [33, 35, 36] are sometimes limited by small scales (discussed above) or, for instance, continuous impingement of the jet that creates a 3D, but steady-state outflow near the surface. In addition to being 3D and localized, downburst velocity records are also non-Gaussian [18, 37, 38].

A summary of several IJ studies with various applications to downburst outflows is presented in Table 1. The listed studies focused typically on the investigation of the flow field in downburst outflows and surface pressures on generic buildings. The prevalence of IJ over the gravity current methods in wind engineering is also noticeable in Table 1. Gravity current experiments provide a more realistic dynamical forcing of downbursts and replicability of some of their thermodynamically driven properties (e.g., baroclinically generated vorticity in the outflow). However, from a wind engineering point of view, the low outflow velocities involved in gravity current experiments due to Froude number mismatch between the experiments and the atmosphere lead to favor the IJ approach. IJ experiments are further subdivided into continuous and pulsed IJs, depending on the duration of the issued jet. Continuous experiments simulate a steady jet flow that is less realistic representation of transient downbursts in respect to the pulsed jet approach. Therefore, the current study adopted this latter approach by means of rapid release and closure of the jet nozzle. In Table 1, the terms translating and stationary refer to the cases when the nozzle that produces the jet is moving parallel to the impinging plate and the cases of a stationary nozzle, respectively. The translation of the impinging jet is adopted to simulate the movement of the cloud that is advected by the mean winds across the cloud depth (not applicable to supercell thunderstorms). Currently, the largest geometric scales of experimentally produced IJ downbursts are achieved in the Wind Engineering, Energy and Environment (WindEEE) Dome [39] at Western University (Canada). The reported geometric scales of downburst-like IJs in this facility are 1:200 and above [40, 41].

It is important to note that most of the studies presented in Table 1 used continuous IJs to replicate downburst outflows. However, this approach suffers from the stationarity of the outflow after the passage of the primary vortex.

On the other hand, several studies opted to simulate downburst-like IJs by introducing certain modifications of the traditional ABL wind tunnel apparatuses [22, 42, 43]. In many cases these approaches managed to accurately replicate downburst velocity records at a particular point in the flow, but they inherently lack the complete 3D flow structure of the starburst outflow that is observed in the real scenario [9, 16]. Also, recently Jubayer et al. [44] used a stationary IJ in the WindEEE Dome with the goal to simulate intermediate winds which are characterized as stationary, but non-Gaussian wind systems [37].

The experimental campaign discussed herein is composed of three separate contributions: (1) the measurements database that is published online in open-access mode [45]; (2) the description of the methodology, instrumentation and measurement grid setup that originate the database [46]; (3) the analysis and interpretation of the data, which is the focus of the current manuscript. The aim of these experiments is to produce and analyze a laboratory data set that generically reproduces full-scale downburst observations and at the same time serves as a calibration set for numerical simulations and analytical models of downburst-like flows. Here, the emphasize is on the vortex dynamics aspects and turbulent flow field characterization. The outcomes of this study, which fall under the umbrella of activities of the project THUNDERR [47], will allow to build a comprehensive, physically realistic, and simply applicable experimental model to adopt in the structural design stage.

Table 1 Experimental studies on IJs with application to downburst outflows. While the list is not exhaustive, it indicates a wide range of experimental approaches and apparatuses used to reconstruct downburst-like IJs

Study	Study's main research focus	D[m]	U_{jet}[m s.$^{-1}$]	Continues (C) or Pulsed (P)	Translating (T) or Stationary (S)	Horizontal (H) or Vertical (V) impingement plane	Approximate geometric scale
Lundgren et al. [48]**	Gravity current simulation of microbursts. Vorticity, turbulence and velocity analysis; as well as scaling methodology	0.045	nr	P	S	H	1:22,200*
Yao and Lundgren [49]**	Investigation of flow field in experimentally produced gravity currents. They demonstrated that the velocity under the vortex is 4 times the velocity of vortex advancement	0.045	nr	P	S	H	1:22,200*
Wood et al. [50]	Velocity characteristics investigated at various positions in the flow over flat terrain, and over simple topographic features	0.31	20	C	S	V	1:1300–1:13,000
Chay and Letchford [33]	Simulating the flow structure in a stationary downburst and obtaining the pressure field on a cube immersed in the flow	0.51	10	C	S	H	1:3000
Letchford and Chay [51]	Simulating the flow structure in a moving downburst and obtaining the transient pressure field on a cube immersed in the flow	0.51	10	C	T	H	1:3000

Table 1 (continued)

Study	Study's main research focus	D[m]	U_{jet}[m s.$^{-1}$]	Continues (C) or Pulsed (P)	Translating (T) or Stationary (S)	Horizontal (H) or Vertical (V) impingement plane	Approximate geometric scale
Choi [52]	Variation of wind velocity with height during real thunderstorms and IJ-like replica in the wind simulator	0.1	nr	C	S	V	1:10,000*
Mason et al. [53]	Flow visualization, wind speed and surface pressure measurements from pulsed IJ	0.51	9	P	S	V	1:3000
Sengupta and Sarkar [54]	Transient loads acting on a cube-shaped building model	0.203	10, 16	C	S	H	1:5000*
Xu and Hangan [34]	Investigating the sensitivity of the orthonormal impinging jets with respect to scale, boundary, and inlet conditions	0.0381, 0.216	2.8, 6.8, 11	C	S	H	1:4600–1:26,200*
Mason et al. [55]	Investigating the peak transient loading conditions on a cubic model submerged in the simulated pulsed downburst flow	0.51	9	P	S	H	1:3000
McConville et al. [35]	Three different methods are examined in order to generate the transient signature of a downburst	1	11.1, 16.13	C, P	S, T	H	1:700–1:1000

Table 1 (continued)

Study	Study's main research focus	D[m]	U_{jet}[m s.$^{-1}$]	Continues (C) or Pulsed (P)	Translating (T) or Stationary (S)	Horizontal (H) or Vertical (V) impingement plane	Approximate geometric scale
Zhang et al. [56]	Surface pressure distributions on two gable-roof building models of different roof angles and high-resolution particle image velocimetry (PIV) measurements	0.6	6.9	C	S	H	1:1670*
Jesson et al. [57]	Simulating the transient aspects of downburst-like flow and investigate pressure distributions and forces over cube and portal framed structures	1	13.7	P	S	H	1:1600
Jubayer et al. [58]	Effects of the building position and orientation with respect to the location of the downburst-like IJ on the surface pressure distribution	3.2	8.5	C	S	H	1:100
Elawady et al. [59]	Dynamic response of a transmission line structure subjected to simulated downburst wind field	3.2	nr	C	S	H	1:50
Romanic et al. [60]	Transient behavior in downburst-like IJs in crossflow	3.2	8.9, 12.3, 16.4	C	S	H	1:320*
Junayed et al. [40]	Mean and turbulent characteristics of several large-scale downburst-like IJs analyzed using Cobra probe and PIV measurements	3.2, 4.5	6.0, 8.5, 8.8, 12.1, 13.5, 19.6	C	S	H	1:250–1:1500

Table 1 (continued)

Study	Study's main research focus	D[m]	U_{jet}[m s.$^{-1}$]	Continues (C) or Pulsed (P)	Translating (T) or Stationary (S)	Horizontal (H) or Vertical (V) impingement plane	Approximate geometric scale
Romanic et al. [41]	Scaling of experimentally produced downbursts	3.2	8.9	P	S	H	1:150–1:1500
Romanic and Hangan [61]	Interaction between downbursts and ambient winds	3.2	8.9, 6.9	C	S	H	1:150–1:1500

The phrase "nr" stands for "not reported"

*Geometric scale was not reported in the original paper, but estimated in this study using a full-scale diameter of downburst downdrafts of 1000 m

**These studies used density driven gravity currents instead of IJs to replicate downburst-like flows

The rest of this article is organized as follows. Section 2 briefly describes the WindEEE Dome facility and experimental setup as reported in Canepa et al. [46]. Canepa et al. [46] also discuss the data processing methodology and tools. In addition, Sect. 2 reports specifications of the flow visualization technology used to qualitatively inspect the generated flow field inside the chamber. Section 3 presents the results of this study together with their discussion. Here, the transient features of the generated downburst outflows, with focus to the primary vortex dynamics, are discussed in relation to the position in the flow field and jet intensity. Statistical analyses on the outflow radial and vertical profiles are provided with important insights into their rapid shift during the passage of the primary vortex. The space and time variation of turbulence characteristics is also investigated. Finally, Sect. 4 provides the main conclusions of this research and outlines the prospects for future work.

2 Experiment setup

All experiments analyzed in this study were carried out in the WindEEE Dome at Western University, Canada. The testing chamber of the facility is pictured in Fig. 1. Hangan et al. [39] describe in detail the laboratory and the generation of stationary and non-stationary flows. WindEEE Dome is a hexagonal chamber of 25 m in diameter surrounded by an outer return chamber of 40 m in diameter. Specifically, downburst flows at the WindEEE Dome are created as IJs using six large fans of diameter 2 m located in the upper chamber of the dome. The nozzle that connects upper and testing chamber is kept closed at first to allow the pressurization of the upper chamber. Opening of the nozzle issues an impinging jet towards the horizontal and flat surface of the testing chamber (Fig. 1). Upon hitting the surface, the flow travels radially outward replicating a downburst-like outflow.

In our study, seven Cobra probes with sampling frequency $f_s = 2500$ Hz were mounted on a vertical stiff mast at heights $z = 0.04$, 0.10, 0.15, 0.20, 0.27, 0.42 and 0.50 m to measure the three flow velocity components. The displacement of the mast at 10 different radial positions r/D (0.2 to 2.0 with incremental step of 0.2), and the assumption of circular symmetry of the produced downburst outflow, allowed to accurately reconstruct the spatiotemporal dynamics of the phenomenon. Downward vertical velocities in the impinging jets produced in our experiments were $W_{\text{jet}} = 8.9$ and 16.4 m s^{-1} at the outlet section of the nozzle. Given their ratio of about 1.8, these two jet intensities are hereafter referred to as DB1.0 and DB1.8, respectively. Each experiment with same radial position of measurement and W_{jet} was repeated 20 times in order to increase the statistical value of the analyses.

The specification of the laboratory and of the downburst-like wind formation, along with a detailed description of the instrumentation and experimental setup, is provided in Canepa et al. [46].

The results throughout the paper will be referred to radial and height locations normalized to the position of maximum radial velocity $\overline{V}$ over the entire flow, that in the following of this paper is found respectively at $r_{\max} = D = 3.2$m and $z_{\max} = 0.1$ m.

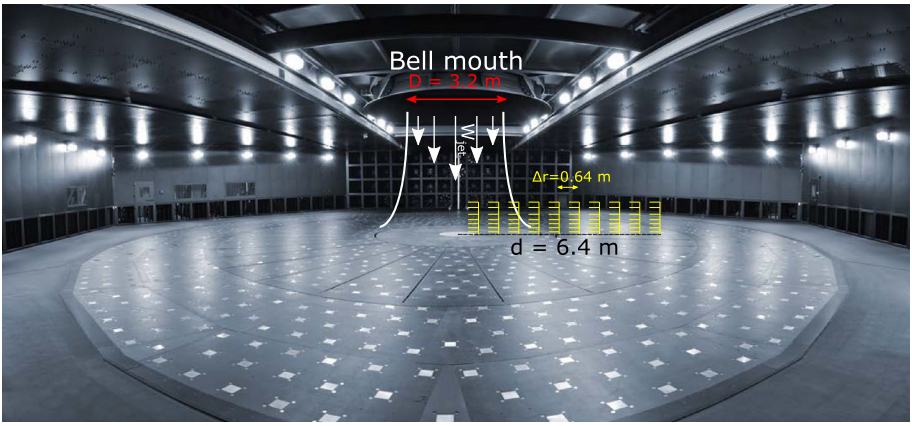

Fig. 1 Testing chamber of the WindEEE Dome with schematic of the downburst-like IJ. Cobra probes' mast is drawn in yellow color at the 10 r/D positions. d is the size of the radial domain of measurements (radial increment $\Delta r = 0.64$ m)

In addition to the Cobra probe velocity measurements, we also performed flow visualization experiments using theatrical fog fluid. These experiments facilitated an overall qualitative interpretation of the downburst outflow evolution in space and time. The visualization smoke is a water-based substance known under the name dipropylene glycol (http://www.ultratecfx.com). The percentage concentration of the composition was always between 60 and 100%. This odorless fluid creates a white cloud of fog with a medium to long hang time. The same seeding material was also used in several PIV measurements in the WindEEEE Dome [40, 62]. A fog machine (Power Fog Industrial 9D by Ultratec Special Effects) with a nozzle and a hose was used to release the fog particles with an average diameter of 1–5 μm into the WindEEE Dome testing chamber prior to the release of the downburst. Afterwards, the visualized outflow was captured using a full-frame digital single-lens reflex (DSLR) camera with the resolution of 1920×1080 pixels. The whole testing chamber was in dark with the exception of two light sheets that were used to illuminate one vertical cross section in the outflow. These two thin sheets of light were created using a couple of oppositely directed stroboscopic machines running in continuous mode. The images were taken at approximately 8 m away from the targeted cross section of downburst outflows and the height of the camera was about 1.6 m above the floor.

3 Results

Canepa et al. [46] showed that a typical downburst record, at least in controlled experimental conditions, consists of three main phases or segments: (1) PV segment, associated with the passage of the primary vortex (PV) over the instrument and this segment is further subdivided into: (1.1) ramp-up of the velocity signal, as PV approaches the instrument; (1.2) the first peak related to the PV and recorded slightly later with respect to its passage over the measuring instrument [9, 40]; (1.3) velocity slowdown as PV travels away from the instrument. (2) Plateau segment, related to the passage of smaller trailing vortices following the PV and characterized by a rather constant ensemble wind speed. The presence and

length of the plateau segment in full-scale records depends on several factors, including the distance between the downdraft and the recording station, the velocity and direction of the downdraft translation (if any) with respect to the station. (3) Dissipation segment, related to the downburst depletion or to the transition of the phenomenon away from the measuring instrument. The analyses and results presented in the current manuscript will be often related to the individual segments of the downburst records. The reader is invited to refer to [46] for further details on the velocity signal phases, including the methodology adopted for their objective identification.

3.1 Primary and secondary vortices

Figure 2a shows the time series of the instantaneous radial velocity V from repetition #12 recorded at the position ($r/r_{max} = 1.6$, $z/z_{max} = 1.0$) for DB1.0 and its moving average $\overline{V}$ evaluated using a moving averaging window $T = 0.1$s [40]. The "secondary" peak occurs at the beginning of the signal enclosed between two dashed black vertical lines. This occurrence is further analyzed using flow visualization of the radially advancing downburst in Fig. 2c,d. The secondary peak is associated with the passage of the secondary vortex (SV) that has an opposite rotation (and vorticity sign) in respect to the PV. The counter-rotating SV that precedes the PV is caused by the dynamic separation-reattachment (bubble) near the surface due to the passage of the PV [40]. The size of the SV and its associated velocities are smaller than those of the PV. The intensity of the secondary peak is proportional to the PV advection velocity, which according to Yao and Lundgren [49] is about four times smaller than the maximum wind speed in the PV. The peak velocity of about 12 m s^{-1} is the result of the superposition of advection velocity and PV circulation relative to the primary vortex center. The secondary peak velocity is about 4 m s^{-1} considering the instantaneous times series, and about 3 m s^{-1} considering its moving average. The sharp decrease of radial wind speed between the time occurrences of SV and PV (see the dashed black vertical line at about 1.7s in Fig. 2a) may be a consequence of the predominantly upward flow between the two vortices, as highlighted by positive values of the vertical velocity w in Fig. 2b. The analysis of the velocity signals shows that the SV is detected for $r/r_{max} \geq 1.2$ and $z/z_{max} > 0.4$. With increasing radial distance, the signature of the SV is more evident at the higher elevations. Indeed, the opposite vorticity in the PV and SV augments the vertical velocity between the vortex pair (see Fig. 2b), which consequently elevates the head of the PV and, in turn, the maximum velocities to higher elevations. Furthermore, the SV is overall less evident in the case DB1.8 where the higher outflow velocities may flatten the SV and therefore make it difficult to be captured.

The SV was also observed in the gravity current experiments of microbursts in Lundgren et al. [48] and Yao and Lundgren [49] and other impinging jet studies [40, 63], as well as in the idealized numerical simulations of Mason et al. [64]. However, the presence of SV is not commonly observed in real downbursts. A weak SV is observed by Sherman [65] in his study of a weak downburst close to Brisbane, Australia, as well as by Romanic [66] in his study of severe microburst recorded on a 213-m tall tower in the Netherlands. The presence of the SV, preceding the passage of the PV, was also reported by Canepa et al. [19] in the downburst event recorded in Genoa on May 13, 2018 by means of a LiDAR vertical profiler. Due to the relative low elevation above the ground of the recorded profile in these real events, the top part of the SV can be hardly captured and, even more so, that of the PV.

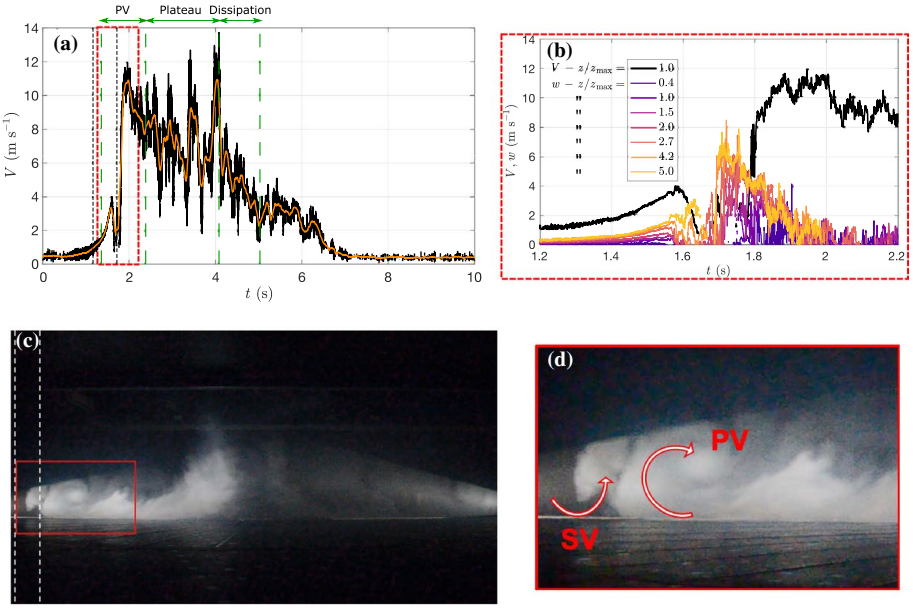

Fig. 2 The secondary vortex (SV) that forms in front of the primary vortex (PV): **a** time series (black line) of the radial wind speed from the repetition #12 at the position ($r/r_{max} = 1.6$, $z/z_{max} = 1.0$) for the case DB1.0 and its moving average (orange line); **b** Zoom in on the time interval between SV and PV (red dashed rectangle in **a**) with reported radial wind speed (black line) and vertical wind speeds (colored lines) at all the instrumented heights and $r/r_{max} = 1.6$; **c** flow visualization of a downburst outflow a few seconds after touchdown; and **d** a zoom in on the frontal zone (the red rectangle in **c**) with the indication of the PV and SV

The duration of ramp-up, plateau and dissipation segments are investigated in Fig. 3 based on the ensemble means of all repetitions. The advection velocity of the approaching PV is proportional to the maximum wind speed in the downburst outflow [48, 67], which, in turn, is proportional to the jet velocity. At the time of maximum outflow intensity, we found that this dependency is described by the relation $\overline{V}_{max} \cong 1.5 \times W_{jet}$. For this reason, the ramp-up period lasts longer in the DB1.0 case compared to DB1.8. Furthermore, the duration of ramp-up can be considered almost constant throughout the radial domain. Assuming that the vorticity in the PV increases while expanding outwards because of vortex stretching, the translational speed has to initially decrease to keep the ramp-up duration constant. Afterwards, flow visualization shows that the size of PV tends to increase and the vorticity of the PV diminishes, in particular when r/r_{max} is larger than $1.4 - 1.6$. Hence, the advection velocity of PV increases further from the touchdown position. From another point of view, the advection velocity of PV can be related to the potential flow model of a vortex ring in proximity to the ground (see, for instance, [68]), which explains the vortex evolution in space and time in terms of interaction between the real vortex and its virtual image placed symmetrically below the ground plane. As the vortex expands outwards, it stretches and increases its rotational speed, while at the same time it also slowly dissipates due to surface drag, entrainment of ambient air, and turbulent viscosity. While stretching increases the rotational speed and hence the PV advection velocity, dissipation terms reduce the rotation and decelerates the PV. The present experiments seem to show that

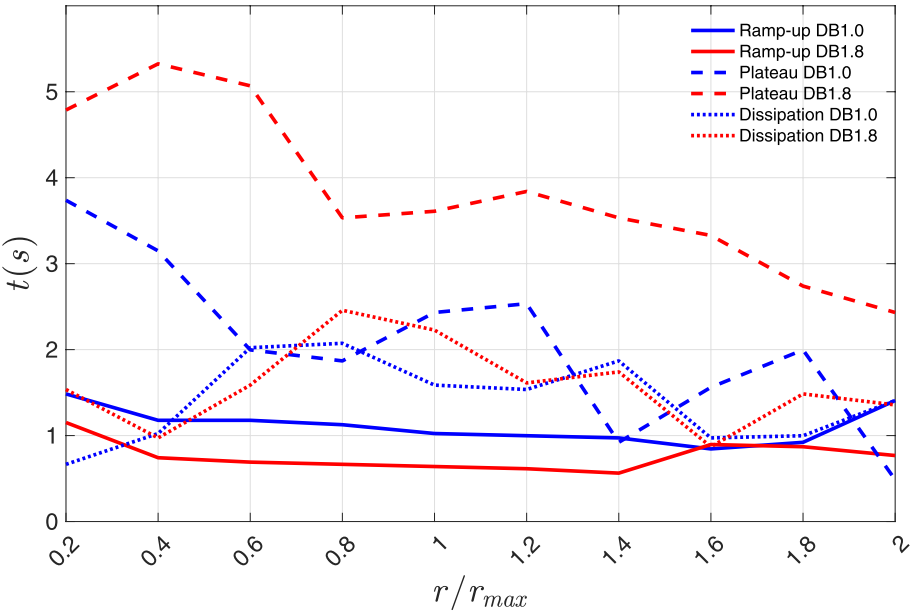

Fig. 3 Duration of ramp-up, plateau and dissipation segments

the former term governs this process up to $r/r_{\max} = 1.4 - 1.6$, whereas the latter contributor becomes more relevant beyond this $r/r_{\max}$. This finding agrees with the experimental results of van Hout et al. [63].

The plateau segment, which is the longest segment of the signals, presents a decreasing trend and is roughly halved along the overall distance of $r/r_{\max} = 2$.

3.2 Radial and vertical velocity profiles

Figure 4 shows for each measurement height the radial profiles of the slowly-varying radial mean velocity, $\overline{V}$, normalized by its maximum value over the entire flow $\overline{\overline{V}}$, at the peak (Fig. 4a,c) and averaged along the plateau segment (Fig. 4b,d). Differently from the absolute maximum of $\overline{V}$ over the entire flow ($\overline{\overline{V}}$), $\overline{V}_{\max}$ hereafter refers to the maximum $\overline{V}$ in the time and/or space subdomain of the measurements. In both cases, the maximum velocities are observed at the lowest two measuring heights and show decreasing trend above. The highest velocities are observed at $r/r_{\max} = 1.0$, which is in accordance with many other experimental studies [e.g., 20, 33, 35]. The wind speed magnitude increases at first with radial distance under the influence of the favorable pressure gradient and, afterwards, decreases because of the viscous dissipation and adverse pressure gradient [69, 70]. Interestingly, the maximum wind speed at the higher heights, i.e. $z/z_{\max} \geq 4.2$, occurs radially closer to the jet touchdown position (around

$r/r_{max} = 0.8$). Nevertheless, during the plateau segment $\overline{V}_{max}$ occurs at $r/r_{max} = 1.0$ only at the lower levels, i.e. $z/z_{max} \leq 1.5$; by increasing the height, $\overline{V}_{max}$ occurs at smaller radial locations. Figure 5 provides an interpretation of this aspect. It shows the vertical profiles of the vertical wind speed $\overline{w}$ for all r/r_{max} measurement positions, at the time of the horizontal velocity peak $t\left(\overline{V}_{max}\right)$ (Fig. 5a,c) and averaged along the plateau segment (Fig. 5b,d). A quite strong downward flow component is observed along the vertical profiles for $r/r_{max} \leq 0.8$. In terms of magnitude, the sharp decrease of $\overline{w}$ from $z/z_{max} = 5.0$ to 0.4 clearly indicates that this area is still inside the downdraft. Upon exiting from the bell mouth, the jet widens in the radial direction beyond its geometric apex, defined by $r/r_{max} = 0.5$, due to the entrainment of ambient air and tangential shear with the surrounding [4, 71]. As the jet approaches the ground, the vertical velocity decreases rapidly while the flow streamlines are forced to spread in the radial direction due to the pressure gradient [6, 69]. This region, where the jet's momentum changes from vertical to horizontal, is named "deflection zone" after Bradshaw and Love [72]. Accordingly, the primary vortex forms at the edge of the downdraft as consequence of the high shear stress with the quiescent and overlying flow, and changes its propagation direction from vertical to horizontal upon the impingement [7]. The maximum radial velocities that are observed at the higher elevations for $r/r_{max} \leq 0.8$ (Fig. 4) are not produced by the passage of the primary vortex; significant horizontal velocities arise in the deflection zone and cause the maxima at these height and radial positions. In the wall-jet region after the impingement, the surface layer thickness is confined underneath the primary vortex [69] and the top measurement heights record a sharp decrease of the velocity magnitude that is clearly detected in Fig. 4a, c and corresponds to the flattening of the top part of the nose-shaped vertical profiles in this stage of the phenomenon. According to the experimental findings of Didden and Ho [70] and Landreth and Adrian [7], the vertical flow reversal highlighted by the positive values of the vertical velocity (upward flow component) for $r/r_{max} \geq 1.0$, indicates the onset of surface layer separation near this point, which corresponds to the formation of the SV at the advancing front of the PV. The highest vertical wind speeds observed at the peak (Fig. 5a, c) at $r/r_{max} = 1.6$ are the result of the strong interaction between the inner-region vortex (SV) formed as consequence of the separation-reattachment of the surface layer, and the outer-region vortex (PV). By moving downstream, the size of the SV increases in height and decreases in the streamwise direction. The coupling with the PV provides a strong upward induction on the SV [73] and high upward flow velocities develop at the boundary between the two vortex structures (see Fig. 2), which eventually induce the SV ejection from the surface. Furthermore, $\overline{w}$ decreases and is very close to 0 for $r/r_{max} = 1.8$ and 2.0. This is consistent with the increasing size of the PV as it spreads out from the touchdown position, while reducing the PV circulation and therefore both the $\overline{V}$ and $\overline{w}$ velocity components. In the plateau segment, $\overline{w}$ is zero for all heights when $r/r_{max} \geq 1.0$, because this region is dominated by smaller-scale random vortices and the mean flow is along horizontal streamlines.

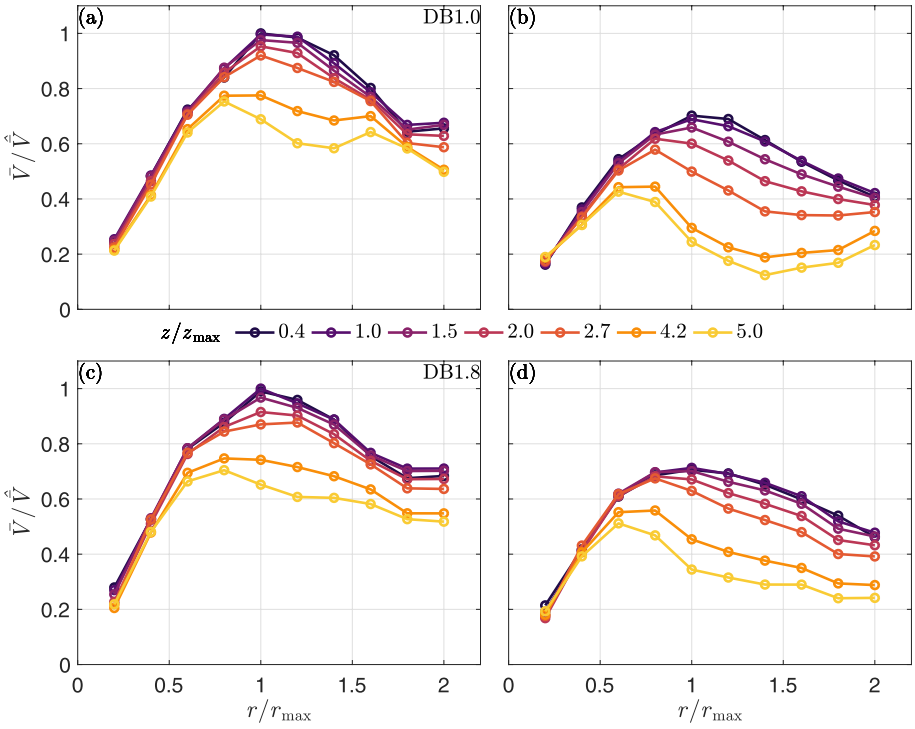

Fig. 4 Radial profiles of normalized radial wind speed: DB1.0 (**a, b**) and DB1.8 (**c, d**) at the peak (**a, c**) and plateau (**b, d**) segments. $\hat{\bar{V}}$ is the maximum value of the slowly-varying radial velocity $\bar{V}$ over the entire flow

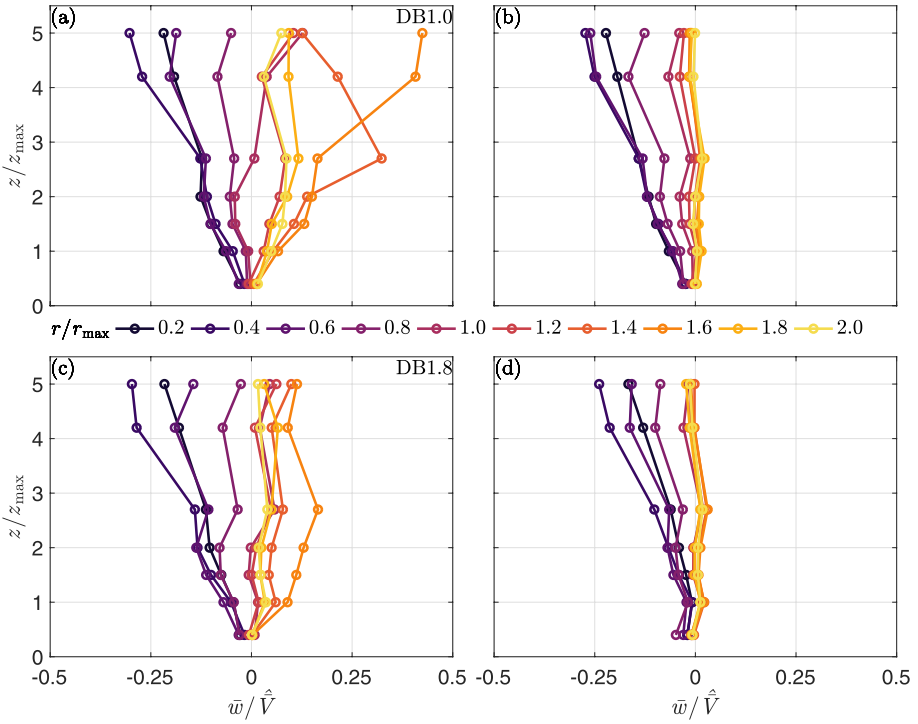

Fig. 5 Vertical profiles of normalized vertical wind speed: DB1.0 (**a, b**) and DB1.8 (**c, d**) at the peak (**a, c**) and plateau (**b, d**) segments of the radial wind speed. $\hat{\overline{V}}$ is the maximum value of the slowly-varying radial velocity $\overline{V}$ over the entire flow

Figure 6 shows the time history of the height of maximum radial slowly-varying mean wind speed $z\left(\overline{V}_{\max}(t)\right)$ along the profile, normalized by $z_{\max}$. $z\left(\overline{V}_{\max}(t)\right)$ is calculated as the ensemble over 20 repetitions at each radial location $r/r_{\max} > 0.8$. Since the main purpose here is to investigate the effect generated by the passage of PV on the height of maximum wind speed, the analysis covers the radial positions outside of the downdraft region (see Fig. 5). While the downburst outflow approaches the instrument

($t < t\left(\overline{V}_{\max}\right)$), the ambient air pushed outwards by the vortex expansion is subjected to an unsteady adverse pressure gradient. Hence, strong viscous effects arise in the near-surface region and provoke the retardation of the flow at the lower levels. At the same time the flow accelerates in the inviscid region farther from the surface and shows rather high velocity gradients [70]. For this reason, the highest wind speeds at the beginning of the velocity ramp-up phase are usually experienced higher above the ground [3]. However, the ramp-up of the velocity time series (orange lines in Fig. 6) is dominated by the subsequent local minimum and maximum of $z\left(\overline{V}_{\max}\right)$ which relate to the formation of the SV in the inner layer of the outflow and to its interaction with the outer layer characterized by the presence of the PV. As a result the maximum velocities develop at the boundary between the two layers [4]. Accordingly, the minimum of $z\left(\overline{V}_{\max}\right)$ increases as the height of SV increases throughout the radial domain of measurements; this corroborates the observations above on the increase of the surface layer thickness by moving away from the jet touchdown. At $r/r_{\max} > 1.6$, the signature of the interaction between PV and SV is experienced almost at the top of the profile, suggesting that the SV is likely to be ejected from the surface. From here, the height of $\overline{V}_{\max}$ decays abruptly and reaches the minimum value of about $z\left(\overline{V}_{\max}\right)/z_{\max} = 0.5$ few instants after $t\left(\overline{V}_{\max}\right)$. $z\left(\overline{V}_{\max}\right)$ appears higher on the ground at radial positions $r/r_{\max} \geq 1.6$ due to the increase of surface layer height. This behavior reflects the transient nature of the downburst outflow and particularly of the travelling vortex which, during its passage, constrains the flow in the area between the vortex lower end and the ground. Our findings demonstrate that the thickness, i.e., height, of the surface layer is both a function of the time and radial position. The theoretical models developed in the literature on this topic neglect the time-dependency of the surface layer thickness and assume the height at which the velocity equals half of the maximum radial velocity as the surface layer characteristic height, constant in time [2, 3, 74–76].

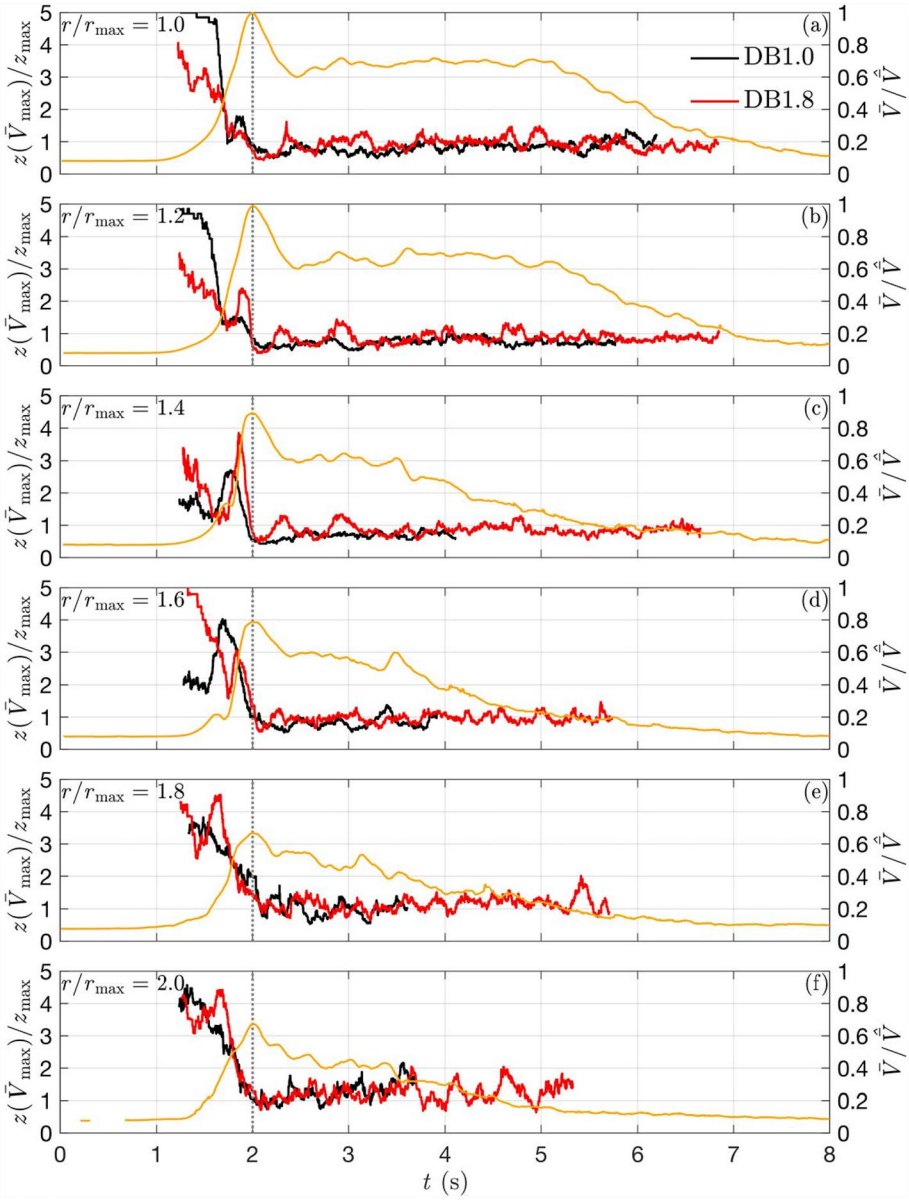

Fig. 6 Ensemble average of 20 experiment repetitions of the height of maximum velocity $z\left(\overline{V}_{\max}\right)$, normalized by $z_{\max} = 0.1$m, for $r/r_{\max} \geq 1.0$ and the cases DB1.0 (black line) and DB1.8 (red line). Orange lines show the ensemble average of the 20 mean wind speed time series at $z/z_{\max} = 1.0$ for the case DB1.0 (shown as reference signal). Vertical gray dotted lines show $t\left(\overline{V}_{\max}\right)$ for the case DB1.0

Figures 7 and 8 provide a thorough characterization of the slowly-varying radial mean velocity field $\overline{V} = \overline{V}(r, z, t)$, calculated as ensemble average across 20 repetitions, in the form $\overline{V} = \overline{V}(z, t)$ and as function of radial positions $0.6 \leq r/r_{\max} \leq 1.6$. The remaining $r/r_{\max}$ locations are not shown here for sake of space but are available in the published database of measurements [45]. The maps of $\overline{V}(z, t)$ show a clear maximum slightly before 2 s, that reaches the highest intensity at $r/r_{\max} = 1.0 - 1.2$. All these maxima correspond to vertical profiles with a clear nose shape. Moving radially outwards, the nose and maximum velocities are gradually constrained to the ground. This is mostly evident in the case DB1.0 for which the PV segment lasts longer because of the lower vortex advection velocity (see Fig. 3). In analogy to Fig. 3, the duration of the plateau segment is observed to decrease with radial distance due to flow dissipation. The transition to dissipation occurs faster in the case DB1.0 due to the lower flow speeds involved.

The spikes in the plateau segment of velocity profiles track the passage of trailing vortices. Underneath the bell mouth's outlet section, Kelvin–Helmholtz instability in the shear layers leads to the formation of vortices with a natural frequency f that is characterized by a Strouhal number St defined in terms of jet velocity W_{jet} and diameter D:

$$St = \frac{f\,D}{W_{\text{jet}}} \tag{1}$$

In an impinging jet, St also depends on Reynolds number Re and nozzle-to-plate height H/D, other than on the initial velocity profile, turbulence state and other factors [77]. In the literature on impinging jets at low Re ($\mathcal{O}(10^4 - 10^5)$) and scales, St is usually found between 0.35–0.65 depending on the parameters above [78–80]. To the authors' knowledge, there are no impinging-jet studies in the literature assessing St for larger Re similar to those tested in the experiments here described (see Sect. 3.3). Considering this range of St, $D = 3.2$m and $W_{\text{jet}} = 8.9\text{m s}^{-1}$ and 16.4m s^{-1}, we obtain a range of vortex shedding frequency $f = 0.97 - 1.81$Hz and $1.79 - 3.33$Hz for DB1.0 and DB1.8, respectively, which, despite being rather wide, qualitatively matches with the occurrence rate of velocity spikes observed in Fig. 7 and Fig. 8.

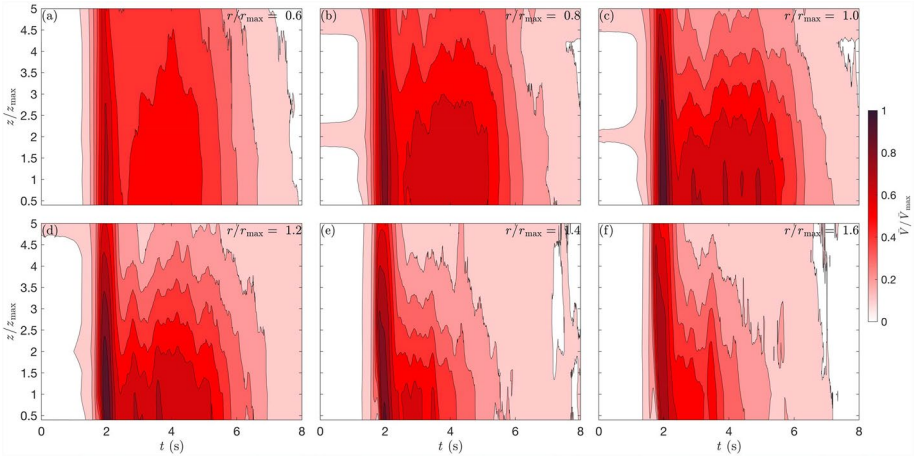

Fig. 7 Profiles of $\overline{V}\left(z/z_{\max}, t\right)$ for $0.6 \leq r/r_{\max} \leq 1.6$ and DB1.0

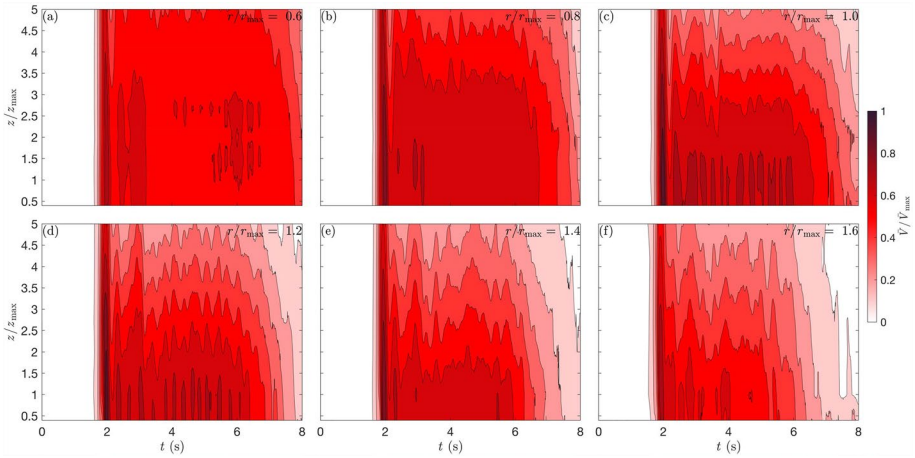

Fig. 8 Profiles of $\overline{V}(z/z_{\max}, t)$ for $0.6 \leq r/r_{\max} \leq 1.6$ and DB1.8

3.3 Turbulence intensity and statistical properties of downburst-like outflows

Several studies reported non-Gaussian properties of full-scale thunderstorm flow fields (see for instance [37]). Figure 9 shows the values of skewness and kurtosis as function of radial and height position for the plateau segment of the records. Because the plateau segment represents the steady-state phase of the outflow, the ensemble mean of multiple repetitions filters out fluctuations around the mean resulting in a nearly Gaussian statistics. The radial location $r/r_{\max} = 0.2$ is horizontally located in proximity of the geometrical downdraft center where the flow has a predominant vertical component; the very little radial velocities detected here cause the related distribution to deviate from the reference Gaussian properties. The same partly holds at the large radial and height locations of measurement, where the flow loses momentum and disperses in a three-dimensional-like pattern. Kurtosis shows a decreasing trend up to $r/r_{\max} = 2.0$, where $\kappa = 2.5$.

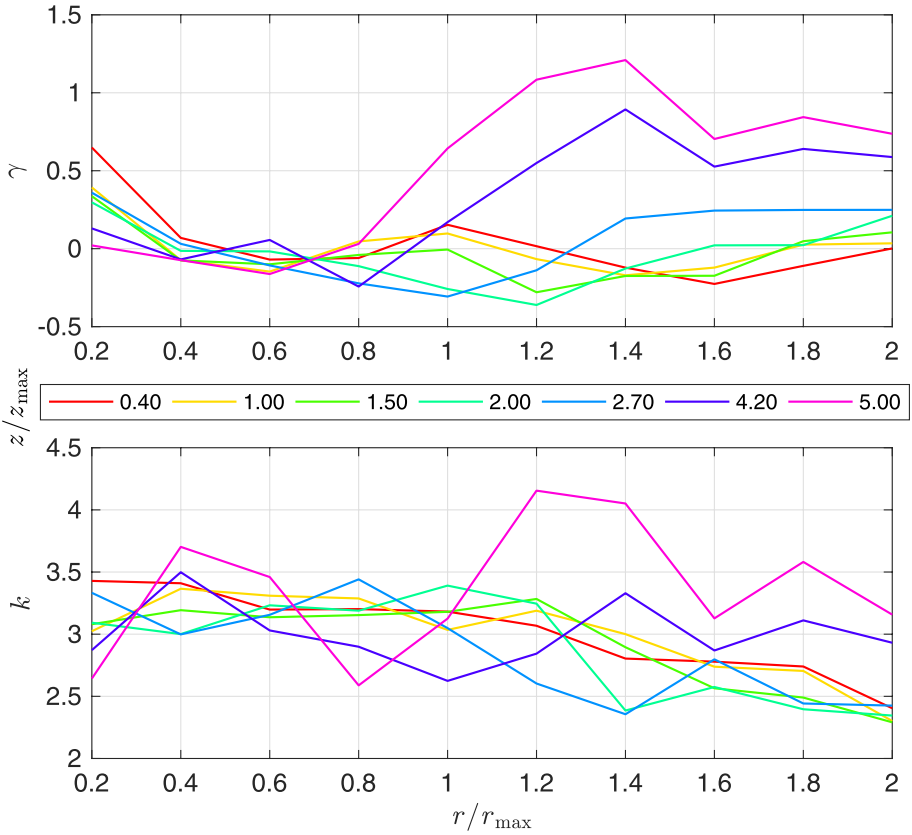

Fig. 9 Dependency of skewness (γ) and kurtosis (k) on height and radial position in the outflow

The velocity histograms for the PV segment are depicted in Fig. 10. Here, the departure from the Gaussian distribution is more pronounced. As expected, velocity PDFs are asymmetric towards high values ($\gamma < 0$) in the area subjected to high radial wind speeds produced by the passage of PV, i.e. $0.8 \leq r/r_{\max} \leq 1.8$ and $0.4 \leq z/z_{\max} \leq 2.7$. Outside this region, the tail of the velocity distribution shifts to low values ($\gamma > 0$). The velocity distributions resemble the Gaussian distribution at radial locations close to the jet touchdown. However, no clear radial trend can be identified.

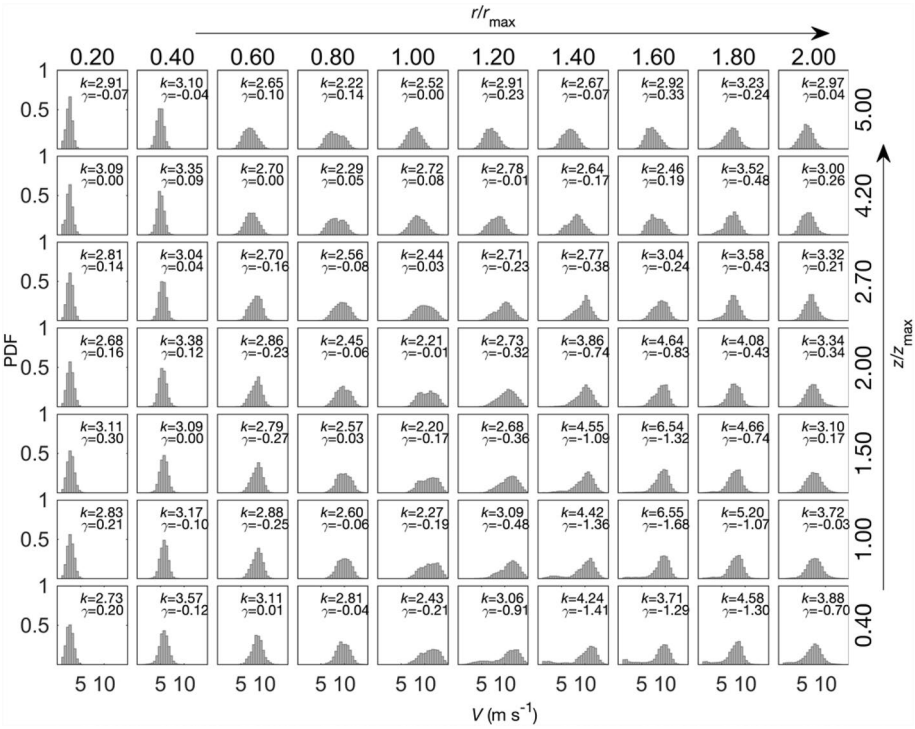

Fig. 10 Velocity histograms of the PV segment (0.25 s on each side of the peak) of 20 downburst outflow repetitions at all heights (z/z_{max}) and radial positions (r/r_{max}), for the case DB1.0. The values of kurtosis (k) and skewness (γ) are included

Table 2 shows the main turbulence properties, averaged along the vertical profile, at all radial locations in the outflow. The measured parameters are:

- Temporal mean $\bar{I}_V(r,z)$ of the slowly varying turbulence intensity $I_V(r,z,t)$ given by:

$$I_V(r,z,t) = \sigma_V(r,z,t)/\overline{V}(r,z,t) \tag{2}$$

$\overline{V}$ is the slowly-varying radial mean velocity extracted applying a moving average period of $T = 0.1$s [40], and σ_V is the slowly-varying standard deviation of the residual turbulent fluctuations, V', given by $V'(r,z,t) = V(r,z,t) - \overline{V}(r,z,t)$. The temporal mean of $I_V(r,z,t)$ was performed over the time interval included between the beginning of the velocity ramp-up period in the PV segment and the final part of the dissipation segment (for reference refer to the instances "1" to "5" in Fig. 4 and Fig. 5 of [46]).

- Skewness $\gamma_{\tilde{V}'}$ and kurtosis $\kappa_{\tilde{V}'}$ of the reduced turbulent fluctuation $\tilde{V}'(r,z,t)$ given by:

$$\tilde{V}'(r,z,t) = V'(r,z,t)/\sigma_V(r,z,t) \tag{3}$$

Similar to Zhang et al. [81] and Canepa et al. [19], extremely large and unphysical values of the turbulence intensity ($I_V > 0.2$) corresponding to very low values of the slowly-varying mean velocity ($\overline{V} < 5$ m s^{-1}) are removed from the analysis.

Table 2 Mean slowly-varying turbulence intensity $\bar{I}_V$; skewness $\gamma_{\tilde{V}'}$; kurtosis $\kappa_{\tilde{V}'}$. The reported values are averaged over all heights

	Case	r/r_{max}									
		0.2	0.4	0.6	0.8	1.0	1.2	1.4	1.6	1.8	2.0
$\bar{I}_V$	DB1.0	0.115	0.092	0.080	0.079	0.084	0.093	0.105	0.117	0.131	0.132
	DB1.8	0.152	0.105	0.085	0.096	0.117	0.138	0.161	0.175	0.183	0.196
$\gamma_{\tilde{V}'}$	DB1.0	0.145	0.040	0.009	0.005	0.034	0.022	− 0.020	0.033	0.051	0.061
	DB1.8	0.109	0.041	− 0.066	− 0.034	0.009	− 0.008	− 0.036	− 0.019	0.055	0.062
$\kappa_{\tilde{V}'}$	DB1.0	2.837	2.909	2.912	2.892	2.874	2.871	2.927	2.840	2.838	2.832
	DB1.8	2.976	3.138	3.211	3.077	2.892	2.854	2.975	2.955	2.772	2.785

The high flow mixing in the jet impingement area contributes to increasing turbulence levels. Outside the downdraft region, i.e., starting from $r/r_{max} = 0.8$, $\bar{I}_V$ increases almost linearly with radial location. At first, the primary vortex leads the downburst outflow and its downward induction has a stabilizing effect on the wall-jet flow [82]. In analogy to Fig. 9, from $r/r_{max} = 1.0$ complex three-dimensional structures emerge and the turbulence intensity increases until the breakaway of the surface layer at large radial distances from the touchdown. $\bar{I}_V$ appears overall greater in the case DB1.8. The ratio between DB1.8 and DB1.0 (not shown here) increases with a quasi-linear trend outside the impingement region up to $r/r_{max} = 1.4$, where the ratio is equal to 1.53. Overall, the turbulence intensity values are in good agreement with those generally found in literature on full-scale downburst events. The recent findings by Canepa et al. [19] on downburst vertical profiles showed that the values of $\bar{I}_V$, averaged along the height, are in the range 0.08–0.09. Solari et al. [83] and Zhang et al. [10, 81] reported $\bar{I}_V = 0.12$ averaged over a large set of downburst outflows extracted from ultrasonic anemometer measurements. In our study, $\bar{I}_V$ averaged along both the height and radial dimensions assumes values of 0.094 and 0.124, respectively for DB1.0 and DB1.8, which is in the range of values obtained from real events in the above studies.

Figure 11 shows the parameter $\mu(r, z, t)$ evaluated as ensemble average of 20 experimental repetitions at each position $r/r_{max} \geq 1.0$ and $z/z_{max} = 0.4, 1.0, 2.0$ and 4.2.

$$\mu(r, z, t) = I_V(r, z, t)/\bar{I}_V(r, z) \tag{4}$$

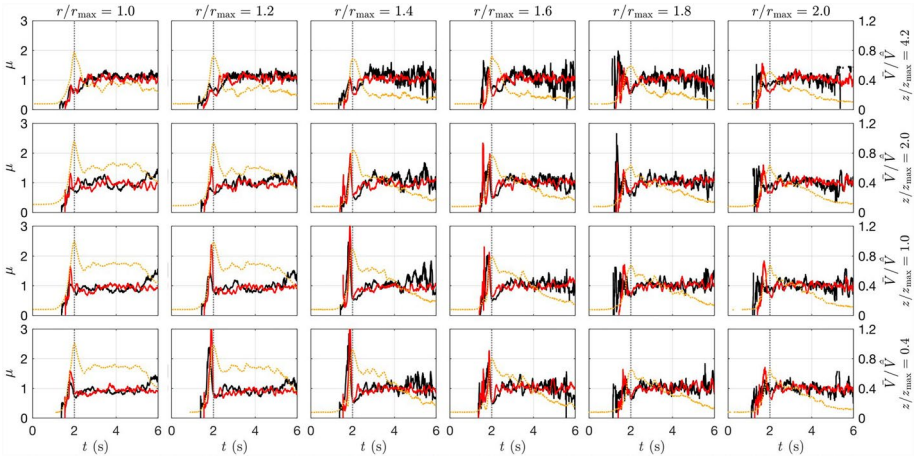

Fig. 11 Ensemble average of 20 experiment repetitions of μ (Eq. 4), for $r/r_{max} \geq 1.0$ and $z/z_{max} = 0.4, 1.0, 2.0, 4.2$ and the cases DB1.0 (black line) and DB1.8 (red line). Orange dotted lines show the ensemble average of 20 mean wind speed time series for the case DB1.0 (shown as reference signal). Vertical gray dotted lines show $t\left(\overline{V}_{max}\right)$

While it is usual practice to assume $\overline{\mu} = 1$, Solari et al. [83] and Zhang et al. [10, 81] noticed asymmetry of $\mu(t)$ around the primary velocity peak, namely in correspondence of the passage of the PV. This asymmetry is more pronounced in the present experiments due to lower Reynolds numbers involved which provide smoother surface compared to the fully turbulent environment in nature. *Re* is here defined as:

$$Re = \frac{W_{jet} D}{\nu} \tag{5}$$

where $\nu = 1.48 \times 10^{-5} \mathrm{m^2 s^{-1}}$ is the kinematic viscosity of air at $15°C$, W_{jet} and D are the jet velocity and diameter, respectively, of either full-scale or experimentally produced downburst. The two cases here investigated, i.e. DB1.0 and DB1.8, provide Reynolds numbers $Re = 1.92 \times 10^6$ and 3.55×10^6, respectively, whereas full-scale downbursts typically present Re in the order of 10^9. The same order of *Re* holds if Re is evaluated as function of the maximum velocity over the entire flow and its height of occurrence, $\overline{V}$ and z_{max}, respectively.

Concurrently with the increase of velocity in the PV segment, μ drastically increases and reaches the maximum shortly before the occurrence of $\overline{V}_{max}$ (vertical gray dotted lines). The maximum value $\mu = 3.28$ is detected at $r/r_{max} = 1.2$ and $z/z_{max} = 0.4$ for the case DB1.8, which shows overall greater values in respect to DB1.0, as expected. In general terms, μ at the peak increases with the radial distance up to $r/r_{max} = 1.4$ and decreases afterwards, while decreasing along the height. Furthermore, a prior spike of μ sometimes higher than that related to $\overline{V}_{max}$, is observed in the range of measurement positions $1.4 \leq r/r_{max} \leq 1.8$ and $0.4 \leq z/z_{max} \leq 2.0$. The domain of observation suggests the correlation with the high shear developed at the boundary between primary and secondary

vortex. Upon reaching the maximum, μ decreases to a local minimum below the unity which is recorded in correspondence of $t\left(\overline{V}_{\max}\right)$ or slightly later. The plateau segment is the longest segment in the velocity records and thus provides the main contribute to the evaluation of $\overline{I}_V$. Accordingly, μ is here close to the unity.

Therefore, in analogy to the full-scale measurements carried out by Zhang et al. [10] and Canepa et al. [19], a sharp peak of the turbulence intensity is observed slightly before the occurrence of the peak velocity. This behavior of μ, observed in both full-scale and controlled conditions, surely represents an important signature of the passage of the PV. The radial and height locations where the asymmetry of μ is clearly recognizable corroborate this observation. As reported above, the maximum values of μ are observed at the radial positions $r/r_{\max} = 1.2 - 1.4$, namely radially further from the location of the recorded maximum wind speed, i.e. $r/r_{\max} = 0.8 - 1.0$ (see Fig. 4). Hjelmfelt [9] first demonstrated that the maximum velocities underneath the vortex follow the vortex center in time and are thus recorded radially behind its location. The same findings are also found in experimentally produced downbursts [40, 67] and seem to be confirmed in our analysis by assuming that the maxima of μ occur concurrently with the passage of PV. For $z/z_{\max} > 2.0$, where the trace of the travelling PV has nearly disappeared, the asymmetric trend of μ is almost lost and the entire signal fluctuates around the mean value $\mu = 1$.

In analogy to Fig. 6, Fig. 12 shows the time evolution of the height of maximum radial turbulence intensity in the wall-jet region, i.e., $r/r_{\max} > 0.8$. At the beginning of velocity ramp-up and for radial positions $r/r_{\max} \leq 1.4$, turbulence is convected to higher levels in the free-shear layer due to the viscous-inviscid interaction [73]. From approximately $r/r_{\max} = 1.4 - 1.6$ the SV forms and turbulence mostly concentrates at the boundary with the PV. Concurrently with the passage of the PV, slightly before the occurrence of the peak velocity (vertical gray dotted lines), $z\left(I_{V_{\max}}\right)$ decreases rapidly to the height of occurrence of the maximum μ observed in Fig. 11, i.e., $z\left(I_{V_{\max}}\right)/z_{\max} < 2$. In correspondence of $t(\overline{V}_{\max})$, as a result of the unsteady adverse pressure gradient induced by the passage of the PV [70], the maxima of turbulence intensity are recorded higher, around $z\left(I_{V_{\max}}\right)/z_{\max} = 4$ throughout the plateau segment of the velocity due to the increase of the surface layer thickness. However, the same behavior is only partly detected at larger radial positions $r/r_{\max} > 1.6$, where the change of $z\left(I_{V_{\max}}\right)$ is less pronounced and the maximum turbulence intensity settles at lower heights.

Overall, the height of maximum turbulence intensity shows a sudden switch in relation to the peak velocity, similarly to what was observed for $z\left(\overline{V}_{\max}\right)$ (Fig. 6). Contrary to $z\left(\overline{V}_{\max}\right)$, however, this change occurs from the lower to the upper heights.

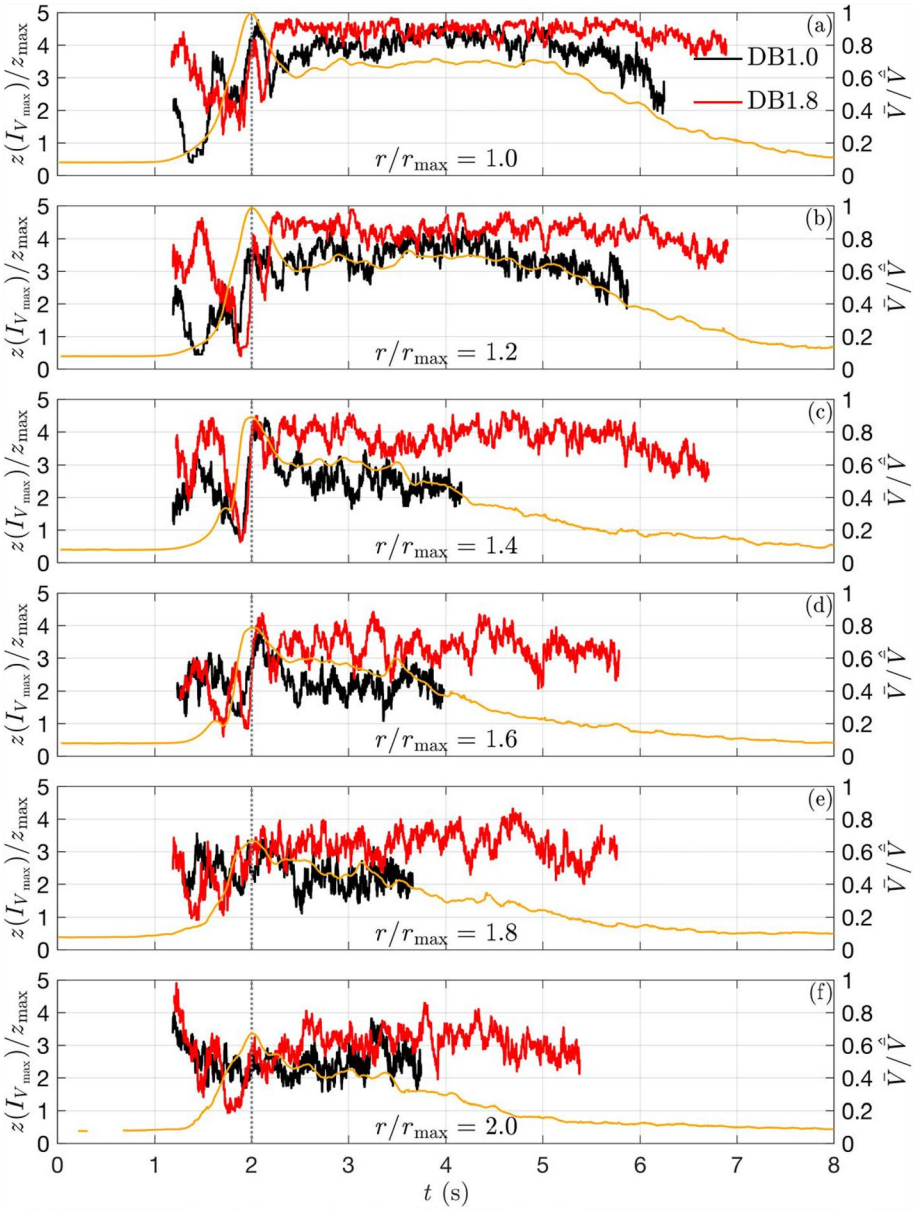

Fig. 12 Ensemble average of 20 experiment repetitions of the height of maximum turbulence intensity $z(I_{V_{max}})$, normalized by $z_{max} = 0.1$m, for $r/r_{max} \geq 1.0$ and the cases DB1.0 (black line) and DB1.8 (red line). Orange lines show the ensemble average of 20 mean wind speed time series at $z/z_{max} = 1.0$ for the case DB1.0 (shown as reference signal). Vertical gray dotted lines show $t\left(\overline{V}_{max}\right)$

Figures 13 and 14 show the profiles of slowly-varying standard deviation and turbulence intensity, $\sigma_V(r, z, t)$ and $I_V(r, z, t)$. The peak of turbulence intensity, mirrored in the standard deviation diagram, is again observed shortly prior to the occurrence of the radial velocity

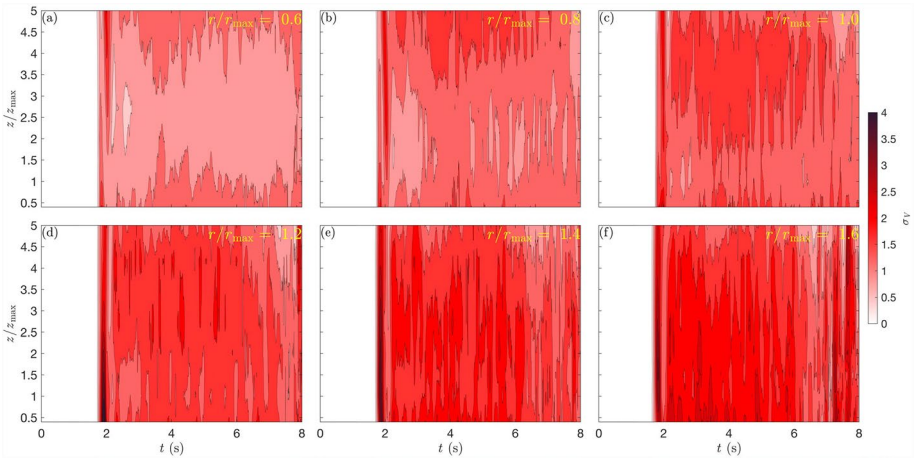

Fig. 13 Profiles of $\sigma_V\left(z/z_{\max}, t\right)$ for $0.6 \leq r/r_{\max} \leq 1.6$ and DB1.8

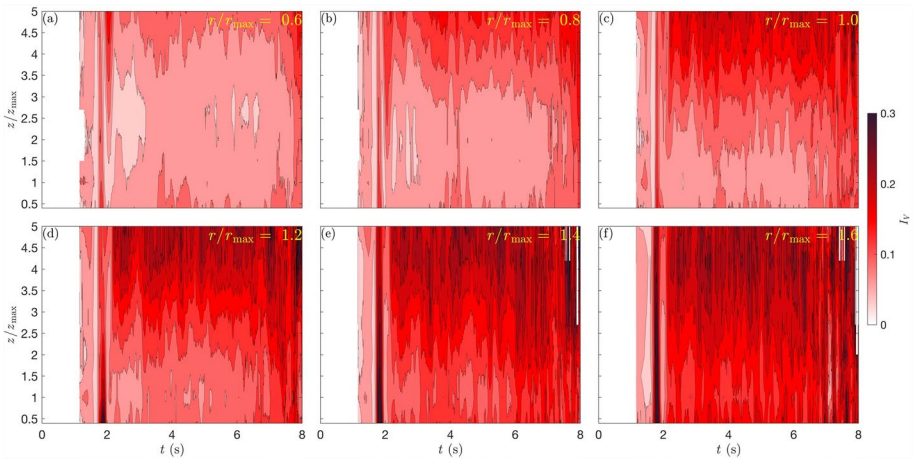

Fig. 14 Profiles of $I_V\left(z/z_{\max}, t\right)$ for $0.6 \leq r/r_{\max} \leq 1.6$ and DB1.8

maxima, corroborating what was assumed above. These peaks gradually grow in magnitude for $r/r_{\max} > 1.0$ and the absolute maxima are detected radially further with respect to the position of maximum wind speed. The vertical profile of I_V, at the time of maximum intensity, shows a nose shape that covers a gradually larger vertical extension by moving along the radial direction. The higher values of I_V at the top of the profile, that are clear for $r/r_{\max} > 1.0$, are caused by the decrease of the radial velocity at those elevations according to the nose-like vertical shape.

Figure 15 shows the Reynolds stress $\overline{u'w'} = \overline{u'w'}(z,t)$ as function of radial coordinate, in analogy to Fig. 7 and Fig. 8, for the case DB1.8. The aim here is to evaluate the momentum flux across the vertical section and provide insights into the flow direction at different elevations above the ground. The change of sign of this parameter eventually identifies the separation between inner and outer surface layer and hence the location of the nose tip of the velocity vertical profile.

The ambient air pushed outwards by the vortex expansion, before the PV segment of the velocity records, is slowed down at the lower elevations because of friction with the ground and assumes a logarithmic-type vertical profile, as shown in Fig. 6. Consequently, the momentum flux is directed downward along the whole vertical extension. With the passage of the PV and subsequent trailing vortices, the surface layer depth reduces and the tip of the nose-shaped profile moves gradually closer to the ground as the vortex advances radially outwards up to $r/r_{\max} = 1.6$. Beyond this location the lifting of the PV (not shown) produces a lift of the separation zone between the two layers. The red area defines the vertical range above the nose of the vertical profile where the velocity gradient is reversed with respect to a boundary layer flow.

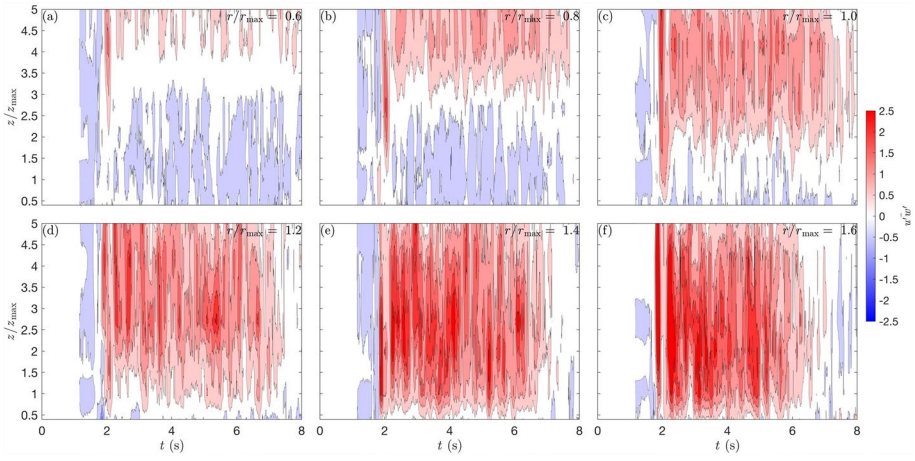

Fig. 15 Profiles of $\overline{u'w'}\left(z/z_{\max}, t\right)$ for $0.6 \leq r/r_{\max} \leq 1.6$ and DB1.8

The Gaussian and stationary properties of the reduced turbulent fluctuations, $\tilde{V}'$ [10, 83], are well retained in the flow generated during our experiments. $\tilde{V}'$ has always nearly zero mean and unit standard deviation; whereas the skewness and kurtosis are close to $\gamma_{\tilde{V}'} = 0$ and $\kappa_{\tilde{V}'} = 3$, respectively. The kurtosis is found to be higher in the case DB1.8, where it shows a quasi-periodic trend with maximum of $\kappa_{\tilde{V}'} = 3.211$ at $r/r_{\max} = 0.6$, while it remains approximately constant around $\kappa_{\tilde{V}'} = 2.9$ for DB1.0. The skewness assumes values $\gamma_{\tilde{V}'} > 0$ within the impingement region while outside of that region fluctuates around zero.

The Kolmogorov's similarity proves that the energy cascade in the inertial subrange is proportional to $n^{-\frac{5}{3}}$, where n is the frequency. In analogy to synoptic ABL winds, several studies in literature on full-scale downburst events demonstrate that the power spectral density (PSD) of $\tilde{V}'$ follows the law $n^{-\frac{5}{3}}$ [18, 83, 84]. Furthermore, Junayed et al. [40] investigated parametrically a set of experimentally produced downburst flows at the WindEEE Dome varying the Reynolds number Re and the ratio H/D, where H is the height of the testing chamber and D the jet diameter. They found that the high frequency end of the spectra of the reduced turbulent fluctuation matches well with the full-scale observations. In particular, the slope $n^{-\frac{5}{3}}$ finds very good fit for large values of Re and $H/D > 1$. The vortex forms fully and the larger range of scales allows a better match with the typical inertial subrange behavior. Figure 16 shows the PSD of $\tilde{V}'$ for DB1.8 which corroborates the observations above.

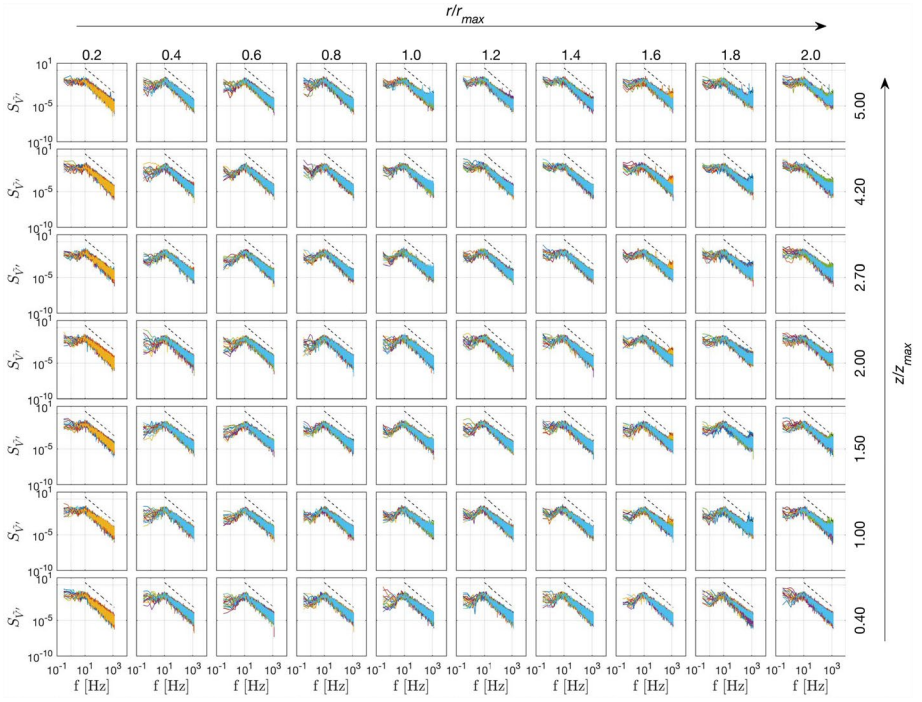

Fig. 16 PSD of the reduced turbulent fluctuation $\tilde{V}'$ for DB1.8, matched with $n^{-\frac{5}{3}}$ profile (dashed lines). Note that the repetition #18 at the radial position $r/D = 0.2$ was excluded from the analyses due to false readings in the measurement record

4 Conclusions and prospects

This paper is an in-depth analysis of a large set of experimentally produced downburst winds at the WindEEE Dome, at Western University in Canada, as part of the project THUNDERR [47]. The aim of this experimental campaign is to produce and analyze a laboratory data set that generically reproduces full-scale observations and at the same time serves as a calibration set for numerical simulations of downburst-like flows. The dynamic characteristics of spatially-stationary, non-steady downburst winds are investigated by means of a refined spatial and temporal grid of Cobra probe measurements at 10 radial positions, 7 vertical positions repeated 20 times to achieve some statistical significance of the results. The database containing all the experimental measurements is published at the online repository PANGAEA [45] and described in detail by Canepa et al. [46]. This latter study shows a new procedure adopted to synchronize the velocity time series among the experimental repetitions.

In order to facilitate comparison with full-scale data collected under the THUNDERR Project, the wind speed records were decomposed into three main segments corresponding to three different time phases observed during full-scale downburst outflows and associated to: (1) passage of the primary vortex; (2) steady state condition, i.e. plateau stage, of the velocity signal; (3) dissipation stage of the downburst. (1) mainly presented asymmetric PDF velocity distributions concentrated towards high values, while (2) showed mostly gaussian properties with the exception of the downdraft region. Frequency peaks are identified as a result of the shear layer instability at the jet exit and can be expressed as a function of the Strouhal number St. The high mixing and three-dimensionality of the flow in the downdraft region and at large radial locations due to surface layer separation, provide an increase of turbulence.

The primary vortex advection velocity depends on the jet intensity and the duration of the ramp-up period changes accordingly. Lower inflow wind speeds cause less energetic primary vortices that dissipate earlier. The secondary vortex often forms ahead of the outflow at large radii as consequence of the dynamic separation-reattachment of the surface layer due to the passage of the primary vortex. The relative large number of experiments allows to statistically address the time evolution of mean radial and vertical outflow profiles. At the beginning of the ramp-up phase of the signals, the maximum wind speed occurs at high heights due to the viscous-inviscid interaction. $z\left(\overline{V}_{\max}\right)$ is then found to increase with radial distance due to the lifting of the interface between primary and secondary vortices. During the primary vortex passage $z\left(\overline{V}_{\max}\right)/z_{\max}$ decreases rapidly to values below 1 and fluctuates around it during the plateau segment. The rapid variation of $z\left(\overline{V}_{\max}\right)$ is thus a consequence of the time-dependency of the surface layer thickness which, at first, is driven by the interaction between primary and secondary vortex and, later, is constrained underneath the passing vortex. At large radii, the surface layer detaches from the surface due to the change of surface-pressure gradient upon the passage of the primary vortex. Previous theoretical models of downburst outflows neglect the time-dependency of the surface layer thickness. The implications of the rapid change of $z\left(\overline{V}_{\max}\right)$ on the structural dynamics deserve future studies.

The values of turbulence intensity match to a very good extent those found for large datasets of real thunderstorm events [10, 19, 81, 83]. The highest values are found shortly prior to the occurrence of the peak wind speed. The peak values of $\mu(t) = I_V(t)/\bar{I}_V$ are observed at radial and vertical locations affected by the primary

vortex passage, $z(I_{V_{max}})/z_{max} < 2$ and $r/r_{max} > 1.0$, respectively. These maxima correspond to nose-like shape vertical profiles with tip covering a larger vertical extension by moving radially outwards. From here, the occurrence of $I_{V_{max}}$ is observed at higher heights due to the unsteady pressure gradient upon the passage of the primary vortex. A first peak of turbulence intensity is sometimes observed at the beginning of the velocity ramp-up and is likely related to the primary-secondary vortex interaction. The rapid change in turbulence intensity reflects the recent findings of Zhang et al. [10, 81] and Canepa et al. [19] on full-scale events where a similar increase and decrease of I_V was observed immediately before and after the occurrence of V_{max}, respectively. This puts into question the usual hypothesis $I_V = \bar{I}_V$ adopted in literature, namely turbulence intensity invariant with time, and may have significant implications on the analysis of the dynamic response of structures to thunderstorm winds. Furthermore, the rapid change of vertical profiles of I_V in correspondence of the passage of the primary vortex emphasizes the transient behavior of downburst winds in terms of wind engineering applications. The asymmetric behavior of μ is found both in controlled experimental conditions and in nature. This may have benefits on the procedures adopted for the systematic detection and extraction of thunderstorm records from large databases of wind measurements. We suggest, therefore, the implementation of μ as well as $z(I_{V_{max}})$ in these techniques.

For the first time, a spatiotemporal (r, z, t) characterization of spatially-stationary non-steady downburst flow fields has been presented, with focus on the slowly-varying mean wind speed and turbulence intensity. The database of measurements published by Canepa et al. [45] and thoroughly described in [46] is here investigated and will form, in addition to parallel CFD and analytical solutions, the skeleton of a refined experimental model to reassess the design codes in terms of fluid–structure interaction.

Future work in the context of the experimental campaign carried out at the WindEEE Dome will address other important aspects of downburst winds. The present experiments are limited to a 2D axisymmetric flow field. In future studies we aim to expand the investigation to 3D by incorporating pointwise azimuthal detections as well as large scale Particle Image Velocimetry (PIV) measurements. A future goal is to reconstruct the complex mechanisms that take place during the occurrence of real downburst events, where the downburst does not develop as isolated system but rather interacts with the background ABL wind and thunderstorm cloud translation. This complex interaction is expected to have important effects on the near-surface outflow impacting on structures. Furthermore, future work will also quantify the effects produced by terrain roughness on downburst winds to achieve a refined and complete physical characterization of this phenomenon.

Acknowledgements This study is supported by the European Research Council (ERC) under the European Union's Horizon 2020 research and innovation program (Grant agreement No. 741273) for the project THUNDERR—Detection, simulation, modelling and loading of thunderstorm outflows to design wind-safer and cost-efficient structures—awarded with an Advanced Grant 2016, as well as by the Canada Foundation for Innovation (CFI) WindEEE Dome Grant (No. X2281B38).

Author contributions FC: Methodology, Software, Validation, Formal analysis, Investigation, Data curation, Writing & editing, Visualization. MB: Conceptualization, Wind tunnel tests, Methodology, Co-supervision, Investigation. DR: Wind tunnel tests, Methodology, Investigation. GS: Conceptualization, Resources, Funding acquisition, Supervision. HH: Resources, Supervision.

Funding Open access funding provided by Università degli Studi di Genova within the CRUI-CARE Agreement. This study is supported by the European Research Council (ERC) under the European Union's Horizon 2020 research and innovation program (grant agreement No. 741273) for the project

THUNDERR—Detection, simulation, modelling and loading of thunderstorm outflows to design wind-safer and cost-efficient structures—awarded with an Advanced Grant 2016, as well as by the Canada Foundation for Innovation (CFI) WindEEE Dome Grant (No. X2281B38).

Availability of data and material The experimental data presented and processed in this research are made available using the data publisher for Earth & Environmental Science PANGAEA (https://www.pangaea.de) [45].

Declarations

Conflict of interest The authors declare that there is no conflict of interest.

References

1. Glauert MB (1956) The wall jet. J Fluid Mech 1:625. https://doi.org/10.1017/S002211205600041X
2. Bakke P (1957) An experimental investigation of a wall jet. J Fluid Mech 2:467–472. https://doi.org/10.1017/S0022112057000270
3. Brady WG, Ludwig G (1963) Theoretical and experimental studies of impinging uniform jets. J Am Helicopter Soc 8:120
4. Gauntner JW, Livingood JNB, Hrycak P (1970) Survey of literature on flow characteristics of a single turbulent jet impinging on a flat plate. NASA Lewis Research Center, Cleveland, OH
5. Bray D, Knowles K (1990) Numerical modeling of an impinging jet in cross-flow. In: 26th joint propulsion conference. American Institute of Aeronautics and Astronautics, Orlando, FL
6. Colucci DW, Viskanta R (1996) Effect of nozzle geometry on local convective heat transfer to a confined impinging air jet. Exp Therm Fluid Sci 13:71–80. https://doi.org/10.1016/0894-1777(96)00015-5
7. Landreth CC, Adrian RJ (1990) Impingement of a low Reynolds number turbulent circular jet onto a flat plate at normal incidence. Exp Fluids 9:74–84. https://doi.org/10.1007/BF00575338
8. Fujita TT (1981) Tornadoes and downbursts in the context of generalized planetary scales. J Atmos Sci 38:1511–1534
9. Hjelmfelt MR (1988) Structure and life cycle of microburst outflows observed in Colorado. J Appl Meteorol 27:900–927
10. Zhang S, Solari G, De Gaetano P et al (2018) A refined analysis of thunderstorm outflow characteristics relevant to the wind loading of structures. Probab Eng Mech 54:9–24. https://doi.org/10.1016/j.probengmech.2017.06.003
11. Fujita TT (1985) The Downburst—Microburst and macroburst—report of projects NIMROD and JAWS
12. Wakimoto RM (1982) The life cycle of thunderstorm gust fronts as viewed with Doppler radar and Rawinsonde data. Mon Weather Rev 110:1060–1082
13. Wakimoto RM, Atkins NT (1991) Wet microburst activity over the southeastern United States: implications for forecasting. Weather Forecast 6:470–482
14. Gast KD, Schroeder JL (2003) Supercell rear-flank downdraft as sampled in the 2002 thunderstorm outflow experiment. In: Proceedings of the eleventh international conference on wind engineering IGWE: Lubbock, Texas
15. Solari G, Repetto MP, Burlando M et al (2012) The wind forecast for safety management of port areas. J Wind Eng Ind Aerodyn 104–106:266–277. https://doi.org/10.1016/j.jweia.2012.03.029
16. Gunter WS, Schroeder JL (2015) High-resolution full-scale measurements of thunderstorm outflow winds. J Wind Eng Ind Aerodyn 138:13–26. https://doi.org/10.1016/j.jweia.2014.12.005

17. Repetto MP, Burlando M, Solari G et al (2018) A web-based GIS platform for the safe management and risk assessment of complex structural and infrastructural systems exposed to wind. Adv Eng Softw 117:29–45. https://doi.org/10.1016/j.advengsoft.2017.03.002
18. Burlando M, Romanić D, Solari G et al (2017) Field data analysis and weather scenario of a downburst event in Livorno, Italy, on 1 October 2012. Mon Weather Rev 145:3507–3527. https://doi.org/10.1175/MWR-D-17-0018.1
19. Canepa F, Burlando M, Solari G (2020) Vertical profile characteristics of thunderstorm outflows. J Wind Eng Ind Aerodyn 206:104332. https://doi.org/10.1016/j.jweia.2020.104332
20. Kim J, Hangan H (2007) Numerical simulations of impinging jets with application to downbursts. J Wind Eng Ind Aerodyn 95:279–298. https://doi.org/10.1016/j.jweia.2006.07.002
21. Sim TS, Ong MC, Quek WY et al (2016) A numerical study of microburst-like wind load acting on different block array configurations using an impinging jet model. J Fluids Struct 61:184–204. https://doi.org/10.1016/j.jfluidstructs.2015.11.002
22. Lin WE, Orf LG, Savory E, Novacco C (2007) Proposed large-scale modelling of the transient features of a downburst outflow. Wind Struct 10:315–346. https://doi.org/10.12989/WAS.2007.10.4.315
23. Mason MS, Wood GS, Fletcher DF (2009) Numerical simulation of downburst winds. J Wind Eng Ind Aerodyn 97:523–539. https://doi.org/10.1016/j.jweia.2009.07.010
24. Orf L, Kantor E, Savory E (2012) Simulation of a downburst-producing thunderstorm using a very high-resolution three-dimensional cloud model. J Wind Eng Ind Aerodyn 104–106:547–557. https://doi.org/10.1016/j.jweia.2012.02.020
25. Lompar M, Ćurić M, Romanic D (2018) Implementation of a gust front head collapse scheme in the WRF numerical model. Atmos Res 203:231–245. https://doi.org/10.1016/j.atmosres.2017.12.018
26. Turner JS (1957) Buoyant vortex rings. Proc R Soc Lond Ser Math Phys Sci 239:61–75
27. Simpson JE (1969) A comparison between laboratory and atmospheric density currents. Q J R Meteorol Soc 95:758–765. https://doi.org/10.1002/qj.49709540609
28. Simpson JE (1972) Effects of the lower boundary on the head of a gravity current. J Fluid Mech 53:759–768. https://doi.org/10.1017/S0022112072000461
29. Charba J (1974) Application of gravity current model to analysis of squall-line gust front. Mon Weather Rev 102:140–156. https://doi.org/10.1175/1520-0493(1974)102%3c0140:AOGCMT%3e2.0.CO;2
30. Jones CS, Cenedese C, Chassignet EP et al (2015) Gravity current propagation up a valley. J Fluid Mech 762:417–434. https://doi.org/10.1017/jfm.2014.627
31. Gutmark E, Wolfshtein M, Wygnanski I (1978) The plane turbulent impinging jet. J Fluid Mech 88:737–756. https://doi.org/10.1017/S0022112078002360
32. Sakakibara J, Hishida K, Phillips WRC (2001) On the vortical structure in a plane impinging jet. J Fluid Mech 434:273–300. https://doi.org/10.1017/S0022112001003779
33. Chay MT, Letchford CW (2002) Pressure distributions on a cube in a simulated thunderstorm downburst—Part A: stationary downburst observations. J Wind Eng Ind Aerodyn 90:711–732. https://doi.org/10.1016/S0167-6105(02)00158-7
34. Xu Z, Hangan H (2008) Scale, boundary and inlet condition effects on impinging jets. J Wind Eng Ind Aerodyn 96:2383–2402. https://doi.org/10.1016/j.jweia.2008.04.002
35. McConville AC, Sterling M, Baker CJ (2009) The physical simulation of thunderstorm downbursts using an impinging jet. Wind Struct 12:133–149. https://doi.org/10.12989/WAS.2009.12.2.133
36. Sengupta A, Haan FL, Sarkar PP, Balaramudu V (2008) Transient loads on buildings in microburst and tornado winds. J Wind Eng Ind Aerodyn 96:2173–2187. https://doi.org/10.1016/j.jweia.2008.02.050
37. De Gaetano P, Repetto MP, Repetto T, Solari G (2014) Separation and classification of extreme wind events from anemometric records. J Wind Eng Ind Aerodyn 126:132–143. https://doi.org/10.1016/j.jweia.2014.01.006
38. Hangan H, Romanic D, Jubayer C (2019) Three-dimensional, non-stationary and non-Gaussian (3D-NS-NG) wind fields and their implications to wind–structure interaction problems. J Fluids Struct 91:102583. https://doi.org/10.1016/j.jfluidstructs.2019.01.024
39. Hangan H, Refan M, Jubayer C et al (2017) Novel techniques in wind engineering. J Wind Eng Ind Aerodyn 171:12–33. https://doi.org/10.1016/j.jweia.2017.09.010
40. Junayed C, Jubayer C, Parvu D et al (2019) Flow field dynamics of large-scale experimentally produced downburst flows. J Wind Eng Ind Aerodyn 188:61–79. https://doi.org/10.1016/j.jweia.2019.02.008
41. Romanic D, Nicolini E, Hangan H et al (2020) A novel approach to scaling experimentally produced downburst-like impinging jet outflows. J Wind Eng Ind Aerodyn 196:104025. https://doi.org/10.1016/j.jweia.2019.104025

42. Lin WE, Savory E (2006) Large-scale quasi-steady modelling of a downburst outflow using a slot jet. Wind Struct 9:419–440. https://doi.org/10.12989/WAS.2006.9.6.419
43. Aboutabikh M, Ghazal T, Chen J et al (2019) Designing a blade-system to generate downburst outflows at boundary layer wind tunnel. J Wind Eng Ind Aerodyn 186:169–191. https://doi.org/10.1016/j.jweia.2019.01.005
44. Jubayer C, Romanic D, Hangan H (2019) Aerodynamic loading of a typical low-rise building for an experimental stationary and non-Gaussian impinging jet. Wind Struct 28:315–329. https://doi.org/10.12989/was.2019.28.5.315
45. Canepa F, Burlando M, Romanic D et al (2021) Downburst-like experimental measurements of two vertical-axis impinging jets at the WindEEE dome. PANGAEA. https://doi.org/10.1594/PANGAEA.931205
46. Canepa F, Burlando M, Romanic D et al (2022) Downburst-like experimental impinging jet measurements at the WindEEE Dome. Nat Sci Data. https://doi.org/10.1038/s41597-022-01342-1
47. Solari G, Burlando M, Repetto MP (2020) Detection, simulation, modelling and loading of thunderstorm outflows to design wind-safer and cost-efficient structures. J Wind Eng Ind Aerodyn 200:104142. https://doi.org/10.1016/j.jweia.2020.104142
48. Lundgren TS, Yao J, Mansour NN (1992) Microburst modelling and scaling. J Fluid Mech 239:461. https://doi.org/10.1017/S002211209200449X
49. Yao J, Lundgren TS (1996) Experimental investigation of microbursts. Exp Fluids 21:17–25. https://doi.org/10.1007/BF00204631
50. Wood GS, Kwok KCS, Motteram NA, Fletcher DF (2001) Physical and numerical modelling of thunderstorm downbursts. J Wind Eng Ind Aerodyn 89:535–552. https://doi.org/10.1016/S0167-6105(00)00090-8
51. Letchford CW, Chay MT (2002) Pressure distributions on a cube in a simulated thunderstorm downburst. Part B: moving downburst observations. J Wind Eng Ind Aerodyn 90:733–753. https://doi.org/10.1016/S0167-6105(02)00163-0
52. Choi ECC (2004) Field measurement and experimental study of wind speed profile during thunderstorms. J Wind Eng Ind Aerodyn 92:275–290. https://doi.org/10.1016/j.jweia.2003.12.001
53. Mason MS, Letchford CW, James DL (2005) Pulsed wall jet simulation of a stationary thunderstorm downburst, Part A: Physical structure and flow field characterization. J Wind Eng Ind Aerodyn 93:557–580. https://doi.org/10.1016/j.jweia.2005.05.006
54. Sengupta A, Sarkar PP (2008) Experimental measurement and numerical simulation of an impinging jet with application to thunderstorm microburst winds. J Wind Eng Ind Aerodyn 96:345–365. https://doi.org/10.1016/j.jweia.2007.09.001
55. Mason MS, James DL, Letchford CW (2009) Wind pressure measurements on a cube subjected to pulsed impinging jet flow. Wind Struct 12:77–88. https://doi.org/10.12989/WAS.2009.12.1.077
56. Zhang Y, Sarkar P, Hu H (2013) An experimental study of flow fields and wind loads on gable-roof building models in microburst-like wind. Exp Fluids 54:1511. https://doi.org/10.1007/s00348-013-1511-9
57. Jesson M, Sterling M, Letchford C, Baker C (2015) Aerodynamic forces on the roofs of low-, mid- and high-rise buildings subject to transient winds. J Wind Eng Ind Aerodyn 143:42–49. https://doi.org/10.1016/j.jweia.2015.04.020
58. Jubayer C, Elatar A, Hangan H (2016) Pressure distributions on a low-rise building in a laboratory simulated downburst. In: Proceedings of the 8th international colloquium on bluff body aerodynamics and applications, Boston, Massachusetts, USA, 10
59. Elawady A, Aboshosha H, El Damatty A et al (2017) Aero-elastic testing of multi-spanned transmission line subjected to downbursts. J Wind Eng Ind Aerodyn 169:194–216. https://doi.org/10.1016/j.jweia.2017.07.010
60. Romanic D, LoTufo J, Hangan H (2019) Transient behavior in impinging jets in crossflow with application to downburst flows. J Wind Eng Ind Aerodyn 184:209–227. https://doi.org/10.1016/j.jweia.2018.11.020
61. Romanic D, Hangan H (2020) Experimental investigation of the interaction between near-surface atmospheric boundary layer winds and downburst outflows. J Wind Eng Ind Aerodyn 205:104323. https://doi.org/10.1016/j.jweia.2020.104323
62. Refan M, Hangan H (2018) Near surface experimental exploration of tornado vortices. J Wind Eng Ind Aerodyn 175:120–135. https://doi.org/10.1016/j.jweia.2018.01.042
63. van Hout R, Rinsky V, Grobman YG (2018) Experimental study of a round jet impinging on a flat surface: flow field and vortex characteristics in the wall jet. Int J Heat Fluid Flow 70:41–58. https://doi.org/10.1016/j.ijheatfluidflow.2018.01.010

64. Mason MS, Fletcher DF, Wood GS (2010) Numerical simulation of idealised three-dimensional downburst wind fields. Eng Struct 32:3558–3570. https://doi.org/10.1016/j.engstruct.2010.07.024
65. Sherman DJ (1987) Weak thunderstorm downburst. Mon Weather Rev 115:1193–1205
66. Romanic D (2021) Mean flow and turbulence characteristics of a nocturnal downburst recorded on a 213 m tall meteorological tower. J Atmospheric Sci. https://doi.org/10.1175/JAS-D-21-0040.1
67. Alahyari A, Longmire EK (1995) Dynamics of experimentally simulated microbursts. AIAA J 33:2128–2136. https://doi.org/10.2514/3.12957
68. Schultz TA (1990) Multiple vortex ring model of the DFW microburst. J Aircr 27:163–168. https://doi.org/10.2514/3.45913
69. Tani I, Komatsu Y (1966) Impingement of a round jet on a flat surface. In: Görtler H (ed) Applied Mechanics. Springer, Berlin, Heidelberg, pp 672–676
70. Didden N, Ho C-M (1985) Unsteady separation in a boundary layer produced by an impinging jet. J Fluid Mech 160:235–256. https://doi.org/10.1017/S0022112085003469
71. Cao G, Kurnitski J, Ruponen M, Seppanen O (2009) Experimental investigation and modeling of the attached plane jet velocity development characteristics in the transition process in a room. HVACR Res 15:489–508. https://doi.org/10.1080/10789669.2009.10390847
72. Bradshaw BA, Love EM (1959) The Normal Impingement of a circular air jet on a flat surface
73. Gogineni S, Shih C (1997) Experimental investigation of the unsteady structure of a transitional plane wall jet. Exp Fluids 23:121–129. https://doi.org/10.1007/s003480050093
74. Poreh M, Tsuei YG, Cermak JE (1967) Investigation of a turbulent radial wall jet. J Appl Mech 34:457–463
75. Oseguera RM, Bowles RL (1988) A simple, analytic 3-dimensional downburst model based on boundary layer stagnation flow. NASA Langley Research Center, Hampton, VA
76. Xu Z, Hangan H, Yu P (2008) Analytical solutions for a family of gaussian impinging jets. J Appl Mech 75:021019. https://doi.org/10.1115/1.2775502
77. Hadžiabdić M, Hanjalić K (2008) Vortical structures and heat transfer in a round impinging jet. J Fluid Mech 596:221–260. https://doi.org/10.1017/S002211200700955X
78. Yule AJ (1978) Large-scale structure in the mixing layer of a round jet. J Fluid Mech 89:413–432. https://doi.org/10.1017/S0022112078002670
79. Tsubokura M, Kobayashi T, Taniguchi N, Jones WP (2003) A numerical study on the eddy structures of impinging jets excited at the inlet. Int J Heat Fluid Flow 24:500–511. https://doi.org/10.1016/S0142-727X(03)00044-4
80. Han B, Goldstein RJ (2003) Instantaneous energy separation in a free jet. Part I. flow measurement and visualization. Int J Heat Mass Transf 46:3975–3981. https://doi.org/10.1016/S0017-9310(03)00245-X
81. Zhang S, Solari G, Burlando M, Yang Q (2019) Directional decomposition and properties of thunderstorm outflows. J Wind Eng Ind Aerodyn 189:71–90. https://doi.org/10.1016/j.jweia.2019.03.014
82. Shih C, Gogineni S (1995) Experimental study of perturbed laminar wall jet. AIAA J 33:559–561. https://doi.org/10.2514/3.12613
83. Solari G, Burlando M, De Gaetano P, Repetto MP (2015) Characteristics of thunderstorms relevant to the wind loading of structures. Wind Struct 20:763–791. https://doi.org/10.12989/WAS.2015.20.6.763
84. Holmes JD, Hangan HM, Schroeder JL et al (2008) A forensic study of the Lubbock-Reese downdraft of 2002. Wind Struct 11:137–152. https://doi.org/10.12989/WAS.2008.11.2.137